Propagación de ondas de choque en la atmósfera solar en la aproximación de dos fluidos

Author
Martín Manuel Gómez Míguez

Tutors
Elena Khomenko Shchukina
Manuel Arturo Collados Vera
Beatrice Annemone Popescu Braileanu
Instituto de Astrofísica de Canarias
Departamento de Astrofísica ULL

Facultad de Ciencias
Universidad de La Laguna

Máster en Astrofísica

Universidad de La Laguna

San Cristóbal de la Laguna , 30 de Junio de 2021

Agradecimientos

Este viaje comenzó hace mucho tiempo. Siendo yo un estudiante de la ESO, estaba ansioso por buscar retos que saciasen mi curiosidad. Fue mi profesora de tecnología, Ana, quien me transmitió su fascinación por la astrofísica y me sugirió venir a las Islas Canarias a formarme. Años después, me convertí en físico en la Universidad de La Laguna y ahora estoy a un pasito de ser astrofísico.

Debo mostrar mi más sincero agradecimiento a todos los compañeros de viaje que he ido haciendo a lo largo de este tiempo y que tanto me han enseñado. En especial, a mis amigos, con los que echarme un café o pasarme horas en apasionantes partidas terraformando Marte; y a mis compañeros de piso (cinco somos), que ya son como una pequeña familia para mí.

Agradezco, como no, la gran labor de mis tutores, de los cuales he aprendido muchísimas cosas y me han hecho sentir como uno más en todo momento.

También agradezco todo el apoyo que he recibido de mi familia. En especial, a mis hermanos, a mi tía, siempre dispuesta ayudarme con cualquier problema; y a la persona que más admiro, mi madre.

Debo dar un agradecimiento más a alguien con quien me habría gustado mucho compartir este momento. *Bótote moito de menos, meu velliño.*

Extended Abstract

Muchos de los fenómenos que tienen lugar en el Sol tienen un impacto directo sobre la vida en La Tierra, por lo que es de gran importancia profundizar en su compresión. Uno de los problemas abiertos en el estudio de la atmósfera solar es el del calentamiento cromosférico. En condiciones de equilibrio radiativo, se espera que la temperatura decrezca con la altura. No obstante, las observaciones muestran la situación opuesta, por lo que deben existir otros mecanismos de transporte energético que justifiquen el incremento de temperatura. Uno de los mecanismos propuestos es el calentamiento por la disipación de energía de ondas, en especial ondas de choque, objeto de estudio en el presente trabajo.

Las condiciones de temperatura y densidad de la cromosfera hacen que esta se comporte como un plasma parcialmente ionizado y que la frecuencia de colisiones entre las distintas especies que lo componen sea órdenes de magnitud inferior menor que en la fotosfera. El campo magnético domina la dinámica del sistema, lo que se conoce como el régimen magnetohidrodinámico. Estos aspectos motivan la descripción de plasma como un sistema formado por dos especies: cargas y neutros. Las cargas, sujetas a la acción del campo magnético, arrastran en su movimiento a los neutros por acoplamiento colisional, los cuales solo están sujetos a fuerzas de empuje y al campo de presiones.

Dado que el Sol y, por tanto, la cromosfera, están formados mayoritariamente por hidrógeno, nos centraremos en la descripción de un plasma de hidrógeno puro bajo el punto de vista del modelo de dos fluidos. Para ello, partimos de la descripción microscópica para un sistema de partículas formado por un número arbitrario de especies, cuya evolución viene dada por la ecuación de Boltzmann. Esta incluye los términos colisionales, que describen la interacción entre las distintas especies. Realizando un promedio estadístico sobre la función de distribución de cada especie, derivamos las magnitudes macroscópicas que describen al sistema, tales como la velocidad promedio, la presión o la temperatura. Los tres primeros momentos de la ecuación de Boltzmann nos conducen a las ecuaciones de conservación de la masa, el momento y la energía. Este sistema de ecuaciones debe ser completado con las ecuaciones que describen el campo magnético, las ecuaciones de Maxwell, además de la ecuación que relaciona la densidad de corriente eléctrica con el campo electromagnético, la ley de Ohm. Las ecuaciones obtenidas serán particularizadas para los modelos de dos fluidos y un fluido.

Si bien la descripción un fluido elimina la presencia de los términos colisionales, introduce un término de autointeracción a través de la ley de Ohm de gran importancia en física solar: la difusividad ambipolar. Este término no está presente en la descripción del modelo de dos fluidos, lo que nos permite confrontar las predicciones de cada modelo y estudiar las limitaciones del modelo de un solo fluido.

Para la realización de los experimentos numéricos, se usó el código Mancha3D-2F, que permite la configuración de simulaciones de dos fluidos y un fluido, desarrollado en el IAC. El acoplamiento de las ecuaciones de dos fluidos hace que tan solo sea posible obtener soluciones analíticas en muy pocos casos, lo que dificulta la comprensión y evaluación de las soluciones numéricas obtenidas. Los experimentos presentados se diseñaron incrementando gradualmente la complejidad de las condiciones físicas, de forma que se puedan estudiar en profundidad los comportamientos introducidos por cada elemento y aislar los efectos numéricos para tratarlos adecuadamente. Nos limitamos al estudio de atmósferas 1D. En primer lugar, se estudia la propagación de ondas acústicas en una atmósfera homogénea. Para su configuración, se genera una perturbación en la base de la atmósfera y se estudia su propagación a lo largo de ella. En este caso, se puede encontrar una solución exacta a las ecuaciones de dos fluidos, que comparamos satisfactoriamente con la solución numérica. Se propone una atmósfera con temperaturas iguales para neutros y cargas y se estudia la relación de dispersión, la cual presenta dos modos y muestra tres regiones diferenciadas: una región de crecimiento del amortiguamiento, otra región de transición y una última región de amortiguamiento saturado. Mientras que la primera

región nos conduce a una solución muy similar a la de un fluido en condiciones de alto acoplamiento, la segunda y la tercera nos muestran la primera de las limitaciones de este planteamiento: el modelo un fluido es una aproximación para frecuencias inferiores a las de colisiones.

En el segundo experimento, incluimos la estratificación por gravedad del medio y usamos como atmósfera de equilibrio el modelo numérico VAL-C, que describe la cromosfera solar. Para comprobar que los resultados fuesen correctos, se estudiaron regímenes de bajas frecuencias y se comparó la solución de dos fluidos con una solución de un fluido y una aproximación analítica que usa como base la solución de una atmósfera isoterma. Para altas frecuencias, se observó el amortiguamiento por colisiones entre neutros y cargas y el impacto del uso de distintas secciones eficaces de colisiones. Se estudió la formación y propagación de ondas de choque y se estudió el peso de los términos colisionales en la ecuación de energía interna, mostrándose mucho más relevantes en la dinámica de las cargas.

En el último bloque de experimentos, se incluyó un campo magnético constante orientado en una dirección perpendicular a la de la atmósfera para poder estudiar la propagación de ondas magnetoacústicas. El campo se ajusta de tal manera que la región de transición entre el régimen hidrodinámico y magnetohidrodinámico su ubique a una cierta altura. En este experimento, confrontamos los efectos colisionales del modelo de dos fluidos con el término ambipolar del modelo de un fluido. Se encuentra que ondas de periodo 5 s se propagan hasta las últimas capas de la cromosfera mientras que las de 1 s apenas logran atravesar la región de transición. También se encuentra que el amortiguamiento ambipolar es mucho más eficiente que el predicho por el modelo de dos fluidos, lo que lleva a que el segundo forme ondas de choque mientras que el primero no, bajo las mismas condiciones. Finalmente, estudiamos el calentamiento neto de la atmósfera con el tiempo para distintas condiciones, obteniendo que las de mayor amplitud y menor frecuencia son las que conducen a un calentamiento más eficiente.

Contents

1 Introduction

The Greeks called the Sun "Helios"; the Romans called it"Sol". The Sun is a G-type main sequence star, a nearly perfect sphere of hot plasma. It is our closest star, therefore, our knowledge of other stars and theoretical models can be improved thanks to its observational accessibility. Solar activity directly affects life on Earth and space weather. Improving our capability to predict energetic events such as coronal mass ejections or strong flares is important due to the emission of dangerous radiation, highly energetic particles and the effects they induce on the increasing number of artificial satellites and geomagnetic storms.

The Sun is a large natural plasma laboratory that can be studied in detail. A plasma is a gas composed by neutral particles (atoms or molecules), ions and free electrons, where the electromagnetic forces play a main role in their behaviour. The stratification of the medium introduced by the solar gravitational field and the extreme temperature and density conditions make the solar plasma a complex system and a challenge from the point of view of theoretical modelling. Fortunately, its observational study of the plasma behaviour is possible because we can spatially resolve its surface in observations.

The Sun is mostly made up of hydrogen (about 92.1% of the number of atoms, 74.9% of the mass), helium (7.8% of the number of atoms and 23.8% of the mass). The remaining 0.1% (about the 2% of the mass) consists of heavier elements, with oxygen (1% of the mass), carbon (0.3%), neon (0.2%) and iron (0.2%) being the most abundant (Hansen & Kawaler, 2012).

1.1 The layers of the Sun's atmosphere

The atmosphere is the outer part of the Sun from where radiation escapes into space. It is composed by three layers: the photosphere, the chromosphere and the corona (see Fig. 1.1).

The photosphere is the deepest layer below which the Sun becomes opaque to the radiation due to the decreasing amount of H^- ions (Gray, 2005). It is about 500 km thick and has approximately a black body spectrum of 6300 K when observed at disk centre. The plasma convection produces granular structures and the magnetic activity leads to the formation of sunspots and other structures.

The chromosphere is above the photosphere and has an extension of 2000 km. The chromospheric spectrum show absortion lines wider than the photospheric ones when it is observed on the disc. Outside the disk, emission lines dominate the spectrum. The chromosphere is usually observed in H_α, one of the strongest lines. It is visible to in the Calcium-K line, a line of CaII in the violet part of the solar spectrum. The temperature grows with height, from 4000 K to 8000 K. Many interesting phenomena can be observed in the chromosphere, which is very complex and dynamic. As an example, one can cite filaments, gigantic clouds of relatively cool gas (in comparison with the surrounding million-degree corona) that rise up from the photosphere and feed coronal mass ejections. Spicules are small jet-like ejections with the appearance of long thin fingers which rise the top of the chromosphere and return to the base.

The temperature continues growing up above the chromosphere from 8000 K to about 500000 K in a very narrow layer, called the transition region. At the top of the atmosphere, the corona reaches temperatures higher than 10^6 K. The density of particles is extremely low, about 10^{12} times less dense than the photosphere. Under these conditions, conventional spectral lines cannot be used to study the corona. It can be better observed in iron emission lines at very high ionization states.

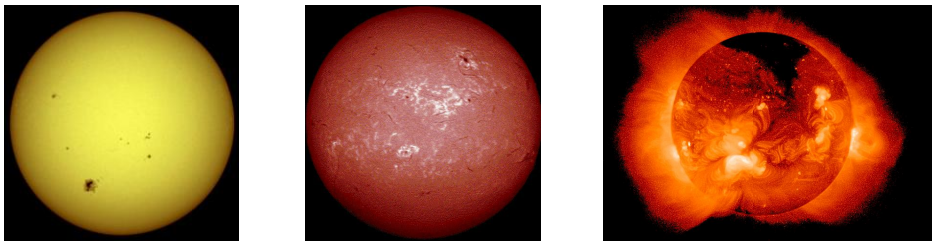

Figure 1.1: From left to right: white light image of the photosphere, H_α image of the chromosphere and X-ray image of the corona. The images were taken from `https://solarscience.msfc.nasa.gov`.

1.2 The problem of the chromospheric heating

If the radiation is the dominant mechanism of energy transport in the chromosphere, the temperature should decrease with the height. Observations shows the opposite situation, the highest layers are hotter than the lowest ones. Therefore, another heating mechanism must exist to explain the observations. Waves have been proposed in this sense, since waves with frequencies in the range of 3-5 mHz are found to dissipate energy in the chromosphere. A review of theoretical studies of wave propagation through the atmospheric layers are shown in Khomenko & Calvo Santamaria (2013) and Khomenko & Collados (2015). The heating by acoustic waves proposed by Biermann (1946) and Schwarzschild (1948) is discussed by Kalkofen (2007). Damping effects become specially important when we consider shock waves. Shocks formed in the chromosphere have been observed (Carlsson & Stein, 2002; Centeno et al., 2009).

There are several non-ideal mechanisms that can damp perturbations, such as viscosity, radiation exchange, thermal conduction or electrical resistivity. All of them can be included in a quasi-MHD description. The damping by ion-neutral friction needs a two-fluid approach to be studied. At the bottom of the chromosphere, the plasma is mainly composed by neutral hydrogen. Since the ionization fraction increases with height and the density decreases, the effects of the interaction between neutrals and charges becomes more important, even more considering that the dynamic of the charges is dominated by the magnetic field, driving the neutrals by the collisional coupling. These conditions motivates the use of a two-fluid approach.

The single-fluid approach deals well with slow processes in partially ionized plasmas, but a two-fluid description is necessary for the relatively fast ones (Zaqarashvili et al., 2011). Here "fast" or "slow" is measured with respect to typical collisional times (see Fig.1.2). When the the time scale of the perturbation is similar to the characteristic time scale of collisions, the momentum transfer between neutrals and charges becomes more efficient, which causes the damping of waves.

1.3 The state of the art

Chromospheric observations generally show that neutrals and charges are coupled. The decoupling effects should be happening at time and spatial scales below the observational resolution. There are only a few direct observations of possible neutral-ion decoupling in solar prominences: the neutral diffusion in prominences modelled by Gilbert et al. (2007) and the indirect evidence obtained by de la Cruz Rodríguez & Socas-Navarro (2011) who deduced misalignment between the magnetic field orientation and the visible direction of chromospheric fibrils.

A more direct measurement can be obtained from the Doppler shift of spectral lines formed by neutral and charged atoms. By observing ion Fe II and neutral Fe I lines simultaneously over the same volume of plasma, differences between ion and neutral velocities of the Evershed flow have been found in sunspot penumbrae as deep as the photosphere by Khomenko et al. (2015). In a similar way, Khomenko et al. (2016) measured Doppler shifts in Ca II 8542 Å and He I 10830 Å emission lines in a solar prominence. The results suggest that the observed differences in velocities are a physical effect

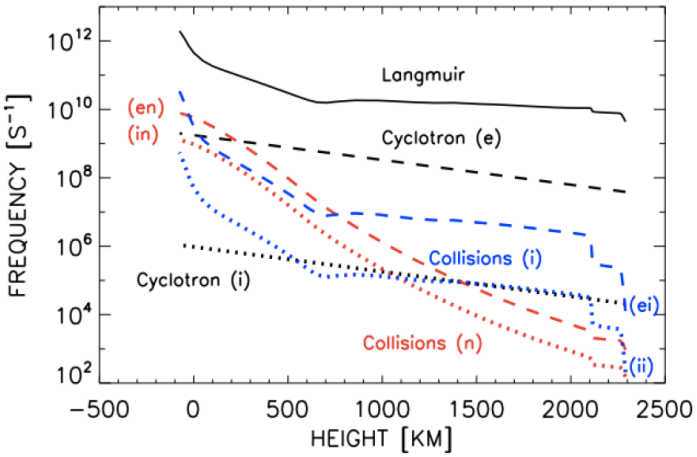

Figure 1.2: Collision, cyclotron and Langmuir frequencies calculated in the Sun atmosphere as a function of height. The species which appear in the plot are: neutrals (n), ions (i), and electrons (e). Part of Fig. 1 from Khomenko et al. (2014a).

and not an observational artifact.

Multi-fluid simulations are far from reproducing realistic situations yet. This is especially true because of the need to consider non-ideal MHD effects, of which we are starting to glimpse their importance and implications. Most numerical models of partially ionized solar plasma use a single-fluid approach, introducing the partial ionization effects through a generalized Ohm's law (Khomenko & Collados Vera, 2012; Cheung & Cameron, 2012; Martínez-Sykora et al., 2012; Khomenko et al., 2014b; Shelyag et al., 2016; Khomenko et al., 2017, 2018). Regarding the two-fluid modeling, Maneva et al. (2017) modeled magneto-acoustic wave propagation in the solar stratified chromosphere including effects of impact ionization and radiative recombination. Martínez-Gómez et al. (2017) study the propagation of waves in a homogeneous plasma in a five-fluid model with two hydrogen components and three helium components. Magnetic reconnection has also been studied in the two-fluid approach (Smith & Sakai, 2008; Leake et al., 2012a; Lukin et al., 2013; Alvarez Laguna et al., 2014; Hillier et al., 2016).

Increasing the number of fluids in the theoretical formalism is not only a computational challenge, it is also difficult from the point of view of the analytic description of the interaction terms and in the configuration of self-consistent equilibrium conditions. The possibility to perform multi-fluid magnetohydrodynamic simulations is still recent and more efforts are necessary to obtain realistic results that can be compared with observations.

2 Objectives

The purpose of this work is to study two-fluid effects in the solar chromosphere in the propagation of monochromatic waves and shock waves. In addition, it can be considered as a validation of the code Mancha-2f (Popescu Braileanu, 2020). Different initial conditions have been used for the test simulations and the results checked with those obtained by Popescu Braileanu (2020). The main objectives pursued in this project were the following:

- **Get familiar with the multifluid plasma description**
- **Study the properties of the collisional terms in the two-fluid approach**
- **Test the code Mancha-2f**
- **Compare the two-fluid and the single-fluid solutions**
- **Develope intuition interpreting numerical results**
- **Study the propagation of waves in the linear regimen**
- **Study the formation and propagation of shock waves**
- **Look for evidence of chromospheric heating due to neutral-charge interaction**

3 Theoretical concepts

3.1 From microscopic to macroscopic plasma description

We consider a plasma composed by different species α. From the point of view of classical mechanics, the instantaneous dynamic state of each particle is determined by its position and velocity, so its movement is properly characterised as a trajectory in the phase space defined by the coordinates $(\vec{r}, \vec{v})$.

Let $\mathcal{N}_\alpha(\vec{r}, \vec{v}, t)$ denote the number of particles of type α inside the volume $d^3r d^3v$ around the phase space coordinates $(\vec{r}, \vec{v})$ at the instant t. The distribution function of each specie, $f_\alpha(\vec{r}, \vec{v}, t)$, is defined as the density of particles inside a differential element of phase space volume:

$$f_\alpha(\vec{r}, \vec{v}, t) = \frac{d^6\mathcal{N}_\alpha(\vec{r}, \vec{v}, t)}{d^3r d^3v} \tag{3.1}$$

This is a function of main relevance in kinetic theory because it provides a complete statistical description of the system and allows us to deduce the macroscopic physical magnitudes.

In the absence of collisions, the system fulfils the conditions of Liouville's theorem (see Bittencourt, 2004) and the time evolution of the distribution function is given by:

$$\frac{\mathcal{D}f_\alpha}{\mathcal{D}t} = \frac{\partial f_\alpha}{\partial t} + \vec{v}\nabla f_\alpha + \vec{a}\nabla_v f_\alpha = 0 \tag{3.2}$$

The operator ∇ is the spatial gradient and ∇_v is the velocity space gradient. In our case, acceleration has the following form,

$$\vec{a} = \vec{g} + \frac{q_\alpha}{m_\alpha}(\vec{v} \times \vec{B} + \vec{E}) \tag{3.3}$$

where q_α is the charge and m_α the mass of the particle of kind α.

Under this consideration, the density of representative points in phase space remains constant in time (Goldstein, 1980). In presence of collisions, particles of type α inside the volume $d^3r d^3v$ at time t may be removed from it at time t' and particles of type α initially outside this volume may end up inside it (Bittencourt, 2004). The net gain or loss of particles of type α as a result of collisions can be introduced as $\left.\frac{\partial f_\alpha(\vec{r},\vec{v},t)}{\partial t}\right|_{coll} d^3r d^3v dt$. This leads from Liouville's equation to Boltzmann's equation,

$$\frac{\mathcal{D}f_\alpha}{\mathcal{D}t} = \left.\frac{\partial f_\alpha}{\partial t}\right|_{coll} \tag{3.4}$$

The description of the equation is incomplete since the form of the collisional term is not provided. An approximation for this term will be discussed at the end of this section.

As we point previously, the distribution function allows us to deduce macroscopic magnitudes from the microscopic variables using statistical mechanics. In this sense, the density of particles is introduced as:

$$n_\alpha(\vec{r}, t) = \int_v f_\alpha(\vec{r}, \vec{v}, t) d^3v \tag{3.5}$$

This definition is especially important because of its statistical meaning; the density of particles is the norm of the marginalized distribution in space and time.

Then, the mean velocity is introduced as:

$$\vec{u}_\alpha(\vec{r},t) = \frac{1}{n_\alpha(\vec{r},t)} \int_v \vec{v} f_\alpha(\vec{r},\vec{v},t) d^3v \tag{3.6}$$

Once this definition is introduced, it is convenient to write the microscopic velocity $\vec{v}$, as the sum of its mean velocity $\vec{u}_\alpha$ and a component whose mean value is null, the random velocity $\vec{c}_\alpha$,

$$\vec{v} = \vec{u}_\alpha + \vec{c}_\alpha \tag{3.7}$$

From this point, we can introduce the other macroscopic fields of interest: the stress tensor and the heat flux[1]:

$$\begin{aligned} \hat{p}_\alpha &= m_\alpha n_\alpha \langle \vec{c}_\alpha \otimes \vec{c}_\alpha \rangle \\ \vec{q}_\alpha &= \frac{1}{2} m_\alpha n_\alpha \langle c_\alpha^2 \vec{c}_\alpha \rangle \end{aligned} \tag{3.8}$$

where the symbol $\otimes$ stands for the external product operation and $\langle\rangle$ denotes the ensemble average defined as:

$$\langle \chi_\alpha(\vec{r},\vec{v},t) \rangle = \frac{1}{n_\alpha(\vec{r},t)} \int_v \chi_\alpha(\vec{r},\vec{v},t) f_\alpha(\vec{r},\vec{v},t) d^3v \tag{3.9}$$

applied to every individual component of the stress tensor and heat flux vector.

The scalar pressure is defined from the stress tensor as:

$$p_\alpha = \frac{1}{3} Tr(\hat{p}_\alpha) \tag{3.10}$$

Finally, the temperature is introduced as

$$p_\alpha = \frac{1}{3} m_\alpha n_\alpha \langle c_\alpha^2 \rangle = n_\alpha k_B T_\alpha \tag{3.11}$$

where k_B is the Boltzmann constant. The velocity distribution of a gas in thermal equilibrium follows a Maxwelian distribution, which does not depend on the direction of velocity and is completely characterized by its temperature.

3.2 Multifluid equations

Once the main thermodynamical fields are introduced, the multi-fluid equations can be shown. According to Khomenko et al. (2014a) and Goedbloed et al. (2019), the zero, first and second moments of Boltzmann equation are given by:

$$\frac{\partial \rho_\alpha}{\partial t} + \nabla(\rho_\alpha \vec{u}_\alpha) = S_\alpha \tag{3.12}$$

$$\frac{\partial(\rho_\alpha \vec{u}_\alpha)}{\partial t} + \nabla(\rho_\alpha \vec{u}_\alpha \otimes \vec{u}_\alpha + \hat{p}_\alpha) = q_\alpha n_\alpha (\vec{E} + \vec{u}_\alpha \times \vec{B}) + \rho_\alpha \vec{g} + \vec{R}_\alpha \tag{3.13}$$

$$\frac{\partial}{\partial t}\left(e_\alpha + \frac{1}{2}\rho_\alpha u_\alpha^2\right) + \nabla\left[\vec{u}_\alpha\left(e_\alpha + \frac{1}{2}\rho_\alpha u_\alpha^2\right) + \hat{p}_\alpha \vec{u}_\alpha + \vec{q}_\alpha\right] = q_\alpha n_\alpha \vec{u}_\alpha \vec{E} + \rho_\alpha \vec{u}_\alpha \vec{g} + M_\alpha \tag{3.14}$$

[1]The notation for electrical charge q_α and heat flux $\vec{q}_\alpha$ may be confuse. If it is necessary to use the modulus of heat flux, it would be denoted by $|\vec{q}_\alpha|$.

The equations includes the internal energy

$$e_\alpha = \frac{p_\alpha}{\gamma - 1} \tag{3.15}$$

with the adiabatic index $\gamma = \frac{5}{3}$ for an ideal monoatomic gas.

Note that when we consider the set of equations for the photons, the conservation equations acquire the particular form of the radiative transfer equations (Mihalas, 1978).

3.2.1 The collisional terms

Collisional terms are defined as follows:

$$\begin{aligned} C_\alpha &= \left.\frac{\partial f_\alpha}{\partial t}\right|_{coll} \\ S_\alpha &= m_\alpha \int_V C_\alpha d^3v \\ \vec{R}_\alpha &= m_\alpha \int_V \vec{v} C_\alpha d^3v \\ M_\alpha &= \frac{1}{2} m_\alpha \int_V v^2 C_\alpha d^3v \end{aligned} \tag{3.16}$$

In order to satisfy the mass, momentum and energy conservation, collisional terms must fulfill the conditions $\sum_\alpha S_\alpha = 0; \sum_\alpha \vec{R}_\alpha = \vec{0}; \sum_\alpha M_\alpha = 0$. They can be split as the sum of an elastic term (for which kinetic energy is conserved) plus an inelastic term. The latter terms are related with processes as ionizations, recombinations or charge exchange (Khomenko et al., 2014a; Braginskii, 1965) which are out of the purposes of our study, so we will focus only on the elastic ones.

A simple method to describe elastic collisional terms is the Krook model approach, also called the relaxation model. It assumes the collisional effects as perturbations that take the system from a state $f_\alpha(\vec{r}, \vec{v}, t)$ to the equilibrium state $f_{\alpha,0}(\vec{r}, \vec{v})$ in a relaxation time $\tau_{\alpha\beta}$ (Bittencourt, 2004) that is related to the characterisitic collisional time between particles α and particles β. The term is given by

$$C_{\alpha\beta}^{elastic} = -\frac{f_\alpha - f_{\alpha,0}}{\tau_{\alpha\beta}} \tag{3.17}$$

where $C_\alpha^{elastic} = \sum_\beta C_{\alpha\beta}^{elastic}$. The collisional frequency can be introduced as $\nu_{\alpha\beta} = \tau_{\alpha\beta}^{-1}$.

As elastic collisions do not lead to the creation or destruction of particles, $S_\alpha^{elastic} = 0$. In the case of the first order elastic collisional term, Braginskii (1965) showed that it can be written as

$$\vec{R}_\alpha^{elastic} = \sum_\beta \rho_\alpha \nu_{\alpha\beta} (\vec{u}_\beta - \vec{u}_\alpha) \tag{3.18}$$

using the Landau approach, a generalization of the Krook approach.

In this latter case, the second order elastic collisional term is shown to be (Braginskii, 1965):

$$M_\alpha^{elastic} = \vec{R}_\alpha^{elastic} + \sum_\beta \left[\vec{u}_\alpha \frac{1}{2} \rho_\alpha \nu_{\alpha\beta} (\vec{u}_\beta - \vec{u}_\alpha)^2 + \frac{1}{2} \rho_\alpha \nu_{\alpha\beta} \left(\frac{3 k_B T_\beta}{m_\beta} - \frac{3 k_B T_\alpha}{m_\alpha} \right) \right] \tag{3.19}$$

The first term is the work done by the momentum collisional term, the second is the frictional heating and the third term is known as thermal exchange.

The collisional frequency can be expressed in terms of the temperature as follows:

$$\nu_{\alpha\beta} = n_\beta \frac{m_\beta}{m_\alpha + m_\beta} \sqrt{\frac{8 k_B T_{\alpha\beta}}{\pi m_{\alpha\beta}}} \sigma_{\alpha\beta}^{elastic} \tag{3.20}$$

where $T_{\alpha\beta} = \frac{T_\alpha + T_\beta}{2}$ can be chosen as reference temperature, $m_{\alpha\beta} = \frac{m_\alpha m_\beta}{m_\alpha + m_\beta}$ and $\sigma_{\alpha\beta}^{elastic}$ is the elastic cross section.

It is important to note that,

$$\rho_\alpha \nu_{\alpha\beta} = \rho_\beta \nu_{\beta\alpha} \tag{3.21}$$

so, generally, $\nu_{\alpha\beta} \neq \nu_{\beta\alpha}$.

3.2.2 Description of electromagnetic field

The system of momentum equations must be closed with the equations that describe the electromagnetic behaviour of the plasma. On one side, the Maxwell equations,

$$\begin{cases} \nabla \cdot \vec{E} = \frac{\sum_\alpha q_\alpha n_\alpha}{\epsilon_0} \\ \nabla \times \vec{E} = -\frac{\partial B}{\partial t} \\ \nabla \cdot \vec{B} = 0 \\ \nabla \times \vec{B} = \mu_0 \vec{J} \end{cases} \tag{3.22}$$

where ϵ_0 is the vacuum permittivity and μ_0 the vacuum permeability. The displacement current term is neglected in Ampère's law, a reasonable assumption for non-relativistic flux. On the other side, the Ohm's law provides an expression to obtain the density current $\vec{J}$, defined as:

$$\vec{J} = \sum_\alpha q_\alpha n_\alpha \vec{u}_\alpha \tag{3.23}$$

Depending on the approach of the study, the way to express the general equation of Ohm's law may be different, according to the particular characteristics of the problem. So, a general and a particular form of Ohm's law in the two-fluid and single-fluid models will be discussed in the following sections.

It is usual to introduce the charge neutrality condition in the plasma definition. In most of the cases, a plasma with a net charge leads to unstable configurations. Mathematically, the condition is expressed as $\sum_\alpha q_\alpha n_\alpha = 0$. This condition will be present in further calculations.

In theoretical descriptions, electromagnetic equations are presented as before. In numerical implementations, the Gauss law for the electric field is not used due to the charge neutrality condition and the electric field is obtained from the Ohm's law. The current density $\vec{J}$ is obtained from the Ampere's law and the induction equation gives an expression for the magnetic field. Nevertheless, small perturbations and numerical oscillations allows local violations of first and third Maxwell equations and they must be checked explicitly by the numerical scheme of the code to ensure the quality of the result.

The set of equations presented until now lay the foundations of the theoretical formalism that sustains our study. In the next sections of the chapter, the particular cases of two-fluid neutral-charge and single-fluid models will be discussed.

3.3 Two fluid equations

Before beginning with the description of the equations, let us to introduce one of the main parameters in plasma physics,

$$\beta_{\text{plasma}} = \frac{p}{p_m} = p \left(\frac{B^2}{2\mu_0} \right)^{-1} \tag{3.24}$$

where p_m is the magnetic pressure.

In case of $\beta_{\text{plasma}} > 1$, the gas pressure dominates over the magnetic pressure, which is called the hydrodynamic regime. This is the case of the solar photosphere. If $\beta_{\text{plasma}} < 1$, the magnetic field dominates the dynamics of the system, which means that we are in the magnetohydrodynamic domain. In solar physics, the region of transition between both cases indicates the beginning of the cromosphere, in which β_{plasma} decreases with the altitude. Under these conditions, a different dynamical behaviour is expected between neutral and charged particles because the former are not affected by the electromagnetic field whilst the latter are dominated by it. This fact motivates a two fluid formalism in which both groups of species are differentiated. The two fluids neutral-charged set of momentum equations was shown to be as follows (Khomenko et al., 2014a; Goedbloed et al., 2019):

$$\frac{\partial \rho_n}{\partial t} + \nabla(\rho_n \vec{u}_n) = S_n \tag{3.25}$$

$$\frac{\partial \rho_c}{\partial t} + \nabla(\rho_c \vec{u}_c) = -S_n \tag{3.26}$$

$$\frac{\partial (\rho_n \vec{u}_n)}{\partial t} + \nabla(\rho_n \vec{u}_n \otimes \vec{u}_n + \hat{p}_n) = \rho_n \vec{g} + \vec{R}_n \tag{3.27}$$

$$\frac{\partial (\rho_c \vec{u}_c)}{\partial t} + \nabla(\rho_c \vec{u}_c \otimes \vec{u}_c + \hat{p}_c) = \vec{J} \times \vec{B} + \rho_c \vec{g} - \vec{R}_n \tag{3.28}$$

$$\frac{\partial}{\partial t}\left(e_n + \frac{1}{2}\rho_n u_n^2\right) + \nabla\left[\vec{u}_n\left(e_n + \frac{1}{2}\rho_n u_n^2\right) + \hat{p}_n \vec{u}_n + \vec{q}_n\right] = \rho_n \vec{u}_n \vec{g} + M_n \tag{3.29}$$

$$\frac{\partial}{\partial t}\left(e_c + \frac{1}{2}\rho_c u_c^2\right) + \nabla\left[\vec{u}_c\left(e_c + \frac{1}{2}\rho_c u_c^2\right) + \hat{p}_c \vec{u}_c + \vec{q}_c\right] = \vec{J}\vec{E} + \rho_c \vec{u}_c \vec{g} - M_n \tag{3.30}$$

Let us denote the group of indices for all species as A. It can be decomposed as $A = A_c \bigcup A_n$, being each subgroup the group of indexes for charges and neutrals, respectively. The velocity of the center of mass for neutrals and charges can be introduced as:

$$\vec{u}_n = \frac{\sum_{\alpha \in A_n} \rho_\alpha \vec{u}_\alpha}{\sum_{\alpha \in A_n} \rho_\alpha}; \qquad \vec{u}_c = \frac{\sum_{\alpha \in A_c} \rho_\alpha \vec{u}_\alpha}{\sum_{\alpha \in A_c} \rho_\alpha} \tag{3.31}$$

The other thermodynamic magnitudes for neutrals and charges can be obtained simply as the corresponding sum over the species of the respective subgroup.

We show the equations for a purely Hydrogen plasma. Regarding the collisional terms, some simplifications must be done in order to make practical use of them (Khomenko et al., 2014a; Popescu Braileanu et al., 2019a). In case of the first moment,

$$\vec{R}_n^{elastic} \approx -(\rho_e \nu_{en} + \rho_i \nu_{in})\vec{w} \tag{3.32}$$

where $\vec{w} = \vec{u}_n - \vec{u}_c$ is the two fluid neutral-charge drift velocity.

Defining the collisional parameter,

$$\alpha = \frac{\rho_e \nu_{en} + \rho_i \nu_{in}}{\rho_n \rho_c} \tag{3.33}$$

such as the effective collision frequencies between charges and neutrals fulfill $\nu_{cn} = \alpha \rho_n$ and $\nu_{nc} = \alpha \rho_c$, the collisional momentum exchange for neutral can be written as:

$$\vec{R}_n^{elastic} = -\alpha \rho_n \rho_c \vec{w} \tag{3.34}$$

$$M_n^{elastic} = -\left[\frac{1}{2}(u_n^2 - u_c^2) + \frac{1}{\gamma - 1}\frac{k_B}{m_n}(T_n - T_c)\right]\alpha\rho_n\rho_c \tag{3.35}$$

The collisional parameter defined as (3.33) is only a function of the average temperature of neutrals and charges,

$$\alpha = \frac{m_{in}}{m_n^2}\sqrt{\frac{8k_BT_{cn}}{\pi m_{in}}}\sigma_{in}^{elastic} + \frac{m_{en}}{m_n^2}\sqrt{\frac{8k_BT_{cn}}{\pi m_{en}}}\sigma_{en}^{elastic} \tag{3.36}$$

considering the constant values $\sigma_{in}^{elastic} = \sigma_{en}^{elastic} \approx 10^{-19}m^2$ (Leake et al., 2012b; Osterbrock, 1961).

Then, let us take a look into the equation of state. For the case of a purely Hydrogen plasma, $n_e = n_i$ as a consequence of charge neutrality. From (3.11), the equations of state for neutrals and charges are given by:

$$p_\alpha = n_\alpha k_B T_\alpha \tag{3.37}$$

In addition, $n_\alpha = \frac{\rho_\alpha}{\mu_\alpha m_n}$, with the average particle mass[2] for neutrals $\mu_n = 1$ and for charges[3] $\mu_c \approx 0.5$, so:

$$p_\alpha = \frac{\rho_\alpha}{\mu_\alpha m_u}k_B T_\alpha \tag{3.38}$$

Another key point of the model is the Ohm's law. In this section, we will take as reference the velocity of the center of mass for charges, so the drift velocity for species of kind α will be defined as:

$$\vec{w}_{\alpha,c} = \vec{u}_\alpha - \vec{u}_c \tag{3.39}$$

The general Ohm's law can be obtained as the weighted sum of the momentum equation of each species with the charge to mass ratio of specie (only charged particles contribute in the sum). Usually, inertial terms of the electron momentum equation are neglected at the beginning of the approach (Khomenko et al., 2014a; Ballester et al., 2018; Braginskii, 1965). In these terms, the equation is shown to be:

$$\begin{aligned}\sum_\alpha \rho_\alpha\left(\frac{q_\alpha}{m_\alpha}\right)^2(\vec{E} + \vec{u}_\alpha \times \vec{B}) = \frac{\partial \vec{J}}{\partial t} + \nabla(\vec{J}\otimes\vec{u}_c + \vec{u}_c\otimes\vec{J}) \\ + \nabla\sum_\alpha\left(\frac{q_\alpha}{m_\alpha}\rho_\alpha\vec{w}_{\alpha,c}\otimes\vec{w}_{\alpha,c}\right) + \sum_\alpha\frac{q_\alpha}{m_\alpha}\nabla\hat{p}_\alpha - \sum\frac{q_\alpha}{m_\alpha}\vec{R}_\alpha\end{aligned} \tag{3.40}$$

The contribution of gravity terms cancels by the charge neutrality. It is important to note that the term $\vec{u}_c \otimes \vec{J}$ was obtained as $\vec{u}_c \otimes \vec{J'}$ but, since the charge neutrality condition,

$$\vec{J'} = \sum_\alpha q_\alpha n_\alpha \vec{w}_{\alpha,c} = \vec{J} \tag{3.41}$$

If we neglect terms proportional to $\frac{m_e}{m_i}$, second order terms and consider stationary currents (Khomenko et al., 2014a; Popescu Braileanu et al., 2019a), the two-fluid Ohm's equation is:

$$\vec{E} + \vec{u}_c \times \vec{B} = \tilde{\eta}_H\vec{J}\times\vec{B} - \tilde{\eta_H}\nabla p_e + \tilde{\eta}\vec{J} + \tilde{\eta}_D\vec{w} \tag{3.42}$$

[2]It is more usual to define the average mass by using the atomic mass unit m_u. By simplicity, we use m_n in our calculus.

[3]We have that $\rho_c = \frac{(m_e+m_n)}{2}n_c \approx \frac{m_n}{2}n_c$.

where

$$\begin{aligned}\tilde{\eta}_H &= \frac{1}{en_e} \\ \tilde{\eta} &= \frac{\rho_e(\nu_{en}+\nu_{ei})}{(en_e)^2} \\ \tilde{\eta}_D &= \frac{\rho_e(\nu_{en}-\nu_{in})}{en_e}\end{aligned} \tag{3.43}$$

with e the electron charge. From right to left in (3.43) the terms are: Hall term, battery term, Ohmic term and the velocity drift term. In this study, an ideal conductor plasma will be considered, so terms on the right must be set to zero.

Since we are interested in the study of heating effects, we write explicitly the internal energy equations:

$$\frac{\partial e_n}{\partial t} + \nabla(\vec{u}_n e_n) + p_n \nabla \vec{u}_n = Q_n \tag{3.44}$$

$$\frac{\partial e_c}{\partial t} + \nabla(\vec{u}_c e_c) + p_c \nabla \vec{u}_c = \vec{J}(\vec{E} + \vec{u}_c \times \vec{B}) + Q_c \tag{3.45}$$

where,

$$Q_n = \frac{1}{2}\alpha\rho_n\rho_c(\vec{u}_n - \vec{u}_c)^2 - \frac{1}{\gamma-1}\frac{k_B}{m_n}\alpha\rho_n\rho_c(T_n - T_c) \tag{3.46}$$

$$Q_c = \frac{1}{2}\alpha\rho_n\rho_c(\vec{u}_n - \vec{u}_c)^2 + \frac{1}{\gamma-1}\frac{k_B}{m_n}\alpha\rho_n\rho_c(T_n - T_c) \tag{3.47}$$

These terms can be understood as a heating flux due to the collisional exchange of energy. It is important to note that, in contrast with the energy collisional terms M_n and M_c (see eq. 3.35), the terms of the internal energy equation are different, the sign of the thermal exchange is positive for neutrals and negative for charges. Generally, in configurations of thermal equilibrium for both species ($T_n = T_c$), the contribution of this term is negligible, so we expect to find $Q_n \approx Q_c$.

3.4 Single fluid equations

In regions where the coupling among the species is high, like in the solar photosphere, the effects of their interaction are weak enough to describe the system as a single fluid, i.e., different species cannot be distinguished. Under this approach, multifluid fluid equations are reduced to (Ballester et al., 2018; Khomenko et al., 2014a):

$$\frac{\partial \rho}{\partial t} + \nabla(\rho\vec{u}) = 0 \tag{3.48}$$

$$\frac{\partial(\rho\vec{u})}{\partial t} + \nabla(\rho\vec{u}\otimes\vec{u} + \hat{p}) = \vec{J}\times\vec{B} + \rho\vec{g} \tag{3.49}$$

$$\frac{\partial}{\partial t}\left(e + \frac{1}{2}\rho u^2\right) + \nabla\left[\vec{u}\left(e + \frac{1}{2}\rho u^2\right) + \hat{p}\vec{u} + \vec{q}\right] = \vec{J}\vec{E} + \rho\vec{u}\vec{g} \tag{3.50}$$

Now, we rewrite the general Ohm's equation (3.40) taking the velocity $\vec{u}$ as reference, and

$$\begin{aligned}\sum_\alpha \rho_\alpha \left(\frac{q_\alpha}{m_\alpha}\right)^2 (\vec{E} + \vec{u}_\alpha \times \vec{B}) = \frac{\partial \vec{J}}{\partial t} + \nabla(\vec{J}\otimes\vec{u} + \vec{u}\otimes\vec{J}) \\ + \nabla\sum_\alpha\left(\frac{q_\alpha}{m_\alpha}\rho_\alpha\vec{w}_\alpha\otimes\vec{w}_\alpha\right) + \sum_\alpha \frac{q_\alpha}{m_\alpha}\nabla\hat{p}_\alpha - \sum\frac{q_\alpha}{m_\alpha}\vec{R}_\alpha\end{aligned} \tag{3.51}$$

with,

$$\vec{w}_\alpha = \vec{u}_\alpha - \vec{u} \tag{3.52}$$

$$\vec{u} = \frac{\rho_n}{\rho}\vec{u}_n + \frac{\rho_c}{\rho}\vec{u}_c = \xi_n\vec{u}_n + \xi_c\vec{u}_c \tag{3.53}$$

where we have defined ξ_n and ξ_c as the density fraction of neutrals and charges. These two magnitudes fulfill that $\xi_n + \xi_c = 1$.

As in the two-fluid model, we neglect second order terms, terms proportional to $\frac{m_e}{m_i}$ and consider stationary currents (Khomenko et al., 2014a). This leads to the equation,

$$\vec{E} + \vec{u} \times \vec{B} = \xi_n(\vec{w} \times \vec{B}) + \tilde{\eta}_H\vec{J} \times \vec{B} - \tilde{\eta_H}\nabla p_e + \tilde{\eta}\vec{J} + \tilde{\eta}_D\vec{w} \tag{3.54}$$

where the following approximation was taken into account:

$$\vec{w}_\alpha \approx \vec{u}_i - \vec{u} = \xi_n(\vec{u}_c - \vec{u}_n) + (\vec{u}_i - \vec{u}_c) \approx -\xi_n\vec{w} \tag{3.55}$$

We need one more step to obtain the single fluid Ohm's law, since (3.54) depends on the drift velocity $\vec{w}$. In order to solve this issue, we sum (3.28) and (3.27) weighted with ξ_n and $-\xi_c$ respectively, obtaining:

$$\xi_n\left(\frac{\partial(\rho_c\vec{u}_c)}{\partial t} + \nabla(\rho_c\vec{u}_c \otimes \vec{u}_c)\right) - \xi_c\left(\frac{\partial(\rho_n\vec{u}_n)}{\partial t} + \nabla(\rho_n\vec{u}_n \otimes \vec{u}_n)\right) = \xi_n[\vec{J} \times \vec{B}] - \vec{G} + \alpha\rho_n\rho_c\vec{w} \tag{3.56}$$

where:

$$\vec{G} = \xi_n\nabla\hat{p}_c - \xi_c\nabla\hat{p}_n \tag{3.57}$$

Again, we can neglect terms on the left side of (3.53), and

$$\vec{w} \approx \frac{\vec{G}}{\alpha\rho_n\rho_c} - \frac{\xi_n}{\alpha\rho_n\rho_c}[\vec{J} \times \vec{B}] \tag{3.58}$$

We can finally obtain the single-fluid Ohm's law by substituting (3.55) in (3.51),

$$\vec{E} + \vec{u} \times \vec{B} = \tilde{\eta}'_H\vec{J} \times \vec{B} - \tilde{\eta}_H\nabla p_e + \tilde{\eta}\vec{J} - \tilde{\eta}_A[(\vec{J} \times \vec{B}) \times \vec{B}] + \tilde{\eta}_G\vec{G} + \tilde{\eta}_{GB}\vec{G} \times \vec{B} \tag{3.59}$$

where:

$$\begin{aligned}
\tilde{\eta}'_H &= \tilde{\eta}_H - \frac{\xi_n}{\alpha\rho_n\rho_c}\eta_D \\
\tilde{\eta}_A &= \frac{\xi_n^2}{\alpha\rho_n\rho_c} \\
\tilde{\eta}_G &= \frac{1}{\alpha\rho_n\rho_c}\tilde{\eta}_D \\
\tilde{\eta}_{GB} &= \frac{\xi_n^2}{\alpha\rho_n\rho_c}
\end{aligned} \tag{3.60}$$

The term proportional to $(\vec{J} \times \vec{B}) \times \vec{B}$ is the single-fluid ambipolar term. It plays an important role in solar atmospheric physics and cannot be ignored in our study. The ambipolar term appears as consequence of the change of the velocity reference system and can be understood as a neutral-charge interaction term in single-fluid modeling since it comes from $\vec{w}$ expression.

It is usual to rewrite the ambipolar coefficient as a ambipolar diffusivity η_A as follows:

$$\tilde{\eta_A} = \eta_A\frac{B^2}{\mu_0} \tag{3.61}$$

As conclusion of the theoretical discussion, both, two-fluid and single-fluid, approaches introduce different terms to model the plasma components interaction. The study of the differences in behaviour predicted in each case motivates the development of the present work, with the aim to find a justification for the chromospheric heating or, at least, part of it.

4 Numerical experiments

4.1 The code Mancha3D 2F

The numerical experiments that support the results of this work were simulated using the Mancha3D-2F code (see Popescu Braileanu, 2020). The code is an extension of Mancha3D (Khomenko & Collados, 2006; Felipe et al., 2010; Khomenko & Collados, 2012; González-Morales et al., 2018), a fully 3D algorithm implemented in Fortran 90 and parallelized with MPI. The variables are split into equilibrium background and perturbation variables, a useful quality for the analysis of results. The code also allows the possibility of solving the fluid equations keeping only the linear terms, so linear and non-linear effects can be distinguished easily. The spatial discretization scheme is fourth-order accurate.

There are three main numerical issues that are critically important in the discussion of the results:

The Perfect Matching Layer (PML): One of the most sensitive factors in a simulation is the boundary conditions. Since the domain volume is finite, one must specify what happens when the flux of some magnitude goes out at the boundary. We will consider that our volume is a fraction of the solar atmosphere, so the point is to emulate that the flux continues its vertical propagation in an extension of our domain. The PML technique allows to avoid reflections at the boundaries (Berenger, 1994; Felipe et al., 2010), which is equivalent to the situation described before. The idea consists of introducing an absorbing layer of a certain width especially designed to absorb without reflections a propagating disturbance that reaches it. In the PML layer, the equations of the conserved magnitudes (the density, the momentum and total energy) are split into three spatial components and an absorbing term proportional to each conserved magnitude component is added. The proportional factor must be calibrated for each configuration.

Hyperdiffusivity: In situations where non-linear effects are important and the characteristic scale of variation of the magnitudes is close to the limit of resolution (for example, in the case of shock waves), some anomalous numerical effects can appear. To deal with the problem, some additional terms are added to momentum equations to correct the non-resolved effects, whose specific form is shown in Popescu Braileanu (2020). The coefficients for each of them must be calibrated in each case.

Filtering: In order to deal with small unresolved scales, additionally to the hyperdiffusivity terms, the solution is periodically filtered using a low pass filtering in order to atenuate the high frequencies.

The strong coupling between neutrals and charges with height leads to large collisional frequencies. This means that, in regions with these properties, like the solar atmosphere, the collisional terms vary in times that are shorter than the hydrodynamic timescales, so they must be implemented carefully to ensure the stability of the solution. To deal with this issue, Mancha3D-2F uses semi-implicit schemes to implement the collisional terms (Popescu Braileanu, 2020).

4.2 First tests: Acoustic waves in a homogeneous plasma

The typical solutions for a single-fluid plasma (homogeneous case, stratified atmosphere, ...) are familiar to the author since they are studied previously in master's degree courses. This is not the case for the two-fluid solutions. To gain intuition on the particular behaviours, we configure different scenarios whose characteristics gradually increase in complexity. This way, the main properties of each

element of the medium can be analyzed in detail separately. We limit our study to 1D configurations along the vertical axis (z-axis) to simplify the expressions and the comprehension of the results.

Neutrals	Charges
$\rho_{n,0} = 9.96 \cdot 10^{-9}\ kg/m^3$	$\rho_{c,0} = 0.25\rho_{n,0} = 1.99 \cdot 10^{-8}\ kg/m^3$
$p_{n,0} = 0.7\ Pa$	$p_{c,0} = 0.5p_{n,0} = 0.35\ Pa$
$c_{n,0} = 7.65 \cdot 10^3\ m/s$	$c_{c,0} = \sqrt{2}c_{n,0} = 1.08 \cdot 10^4\ m/s$
$T_{n,0} = 4259\ K$	$T_{c,0} = T_{n,0} = 4259\ K$

Table 4.1: Values of the background atmosphere used in the tests of the wave propagation in a uniform plasma.

In the first place, we study the propagation of acoustic waves in a homogeneous atmosphere. An analytical solution can be found for the linearized system of equations under some considerations. Let us begin linearizing the two-fluid equations, considering a null magnetic field, a null heat flux and only elastic collisions. Regarding the collisional terms M_α, we initially choose $T_n = T_c$ to reduce its contribution, so that they can be neglected. We split a field f as $f = f_0 + f_1$, where the sub-index 0 denotes the equilibrium field and the sub-index 1 the perturbed field, which must fulfil that $\frac{|f_1|}{f_0} \ll 1$. The equilibrium state is defined by the following relations:

$$u_{n,0} = u_{c,0} = 0; \qquad \frac{\partial \rho_{n,0}}{\partial z} = \frac{\partial \rho_{c,0}}{\partial z} = 0; \qquad \frac{\partial p_{n,0}}{\partial z} = \frac{\partial p_{c,0}}{\partial z} = 0 \tag{4.1}$$

Since we consider a static equilibrium case, $u_n = u_{n,1}$ and $u_c = u_{c,1}$. From now on, we will use the forms shown at the left hand side to denote the perturbed state to simplify the notation. This will be the case for all the configurations proposed in this work and this criterion will be used again. The description of the equilibrium state is completed with the relations obtained from the momentum equations. If we consider only the equilibrium fields and substitute (4.1) in (3.25), (3.26) and then combine the result with (3.29) and (3.30), we obtain respectively:

$$\frac{\partial \rho_{n,0}}{\partial t} = \frac{\partial \rho_{c,0}}{\partial t} = 0; \qquad \frac{\partial p_{n,0}}{\partial t} = \frac{\partial p_{c,0}}{\partial t} = 0 \tag{4.2}$$

Then, we can begin with the linearization of the equations, taking only the first-order terms. For the mass conservation equations (3.25) and (3.26):

$$\frac{\partial(\rho_{\alpha,0} + \rho_{\alpha,1})}{\partial t} + \frac{\partial[(\rho_{\alpha,0} + \rho_{\alpha,1})u_\alpha]}{\partial z} = 0 \ \Rightarrow\ \frac{\partial \rho_{\alpha,1}}{\partial t} + \rho_{\alpha,0}\frac{\partial u_\alpha}{\partial t} = 0 \tag{4.3}$$

As general rule in this chapter, we will use the sub-index alpha to show results and deductions that are the same for neutrals and charges.

We continue with the momentum conservation equations, from (3.27) and (3.28):

$$\begin{aligned} \frac{\partial[(\rho_{\alpha,0} + \rho_{\alpha,1})u_\alpha]}{\partial t} + \frac{\partial[(\rho_{\alpha,0} + \rho_{\alpha,1})u_\alpha^2]}{\partial z} + \frac{\partial(p_{\alpha,0} + p_{\alpha,1})}{\partial z} &= -\varepsilon_\alpha(\alpha_0 + \alpha_1)(\rho_{n,0} + \rho_{n,1})(\rho_{c,0} + \rho_{c,1})w \\ \Rightarrow\ \rho_{\alpha,0}\frac{\partial u_\alpha}{\partial t} + \frac{\partial p_{\alpha,1}}{\partial z} &= -\varepsilon_\alpha \alpha_0 \rho_{n,0}\rho_{c,0} w \end{aligned} \tag{4.4}$$

where we introduce $\varepsilon_n = 1$ and $\varepsilon_c = -1$ to write the equations for neutrals and charges in one expression.

And finally, we linearize the energy conservation equations from (3.29) and (3.30):

$$\begin{aligned}
&\frac{\partial}{\partial t}\left[\frac{1}{\gamma-1}(p_{\alpha,0}+p_{\alpha,1})+\frac{1}{2}(\rho_{\alpha,0}+\rho_{\alpha,1})u_\alpha^2\right]+\frac{\partial}{\partial z}\left[\frac{\gamma}{\gamma-1}(p_{\alpha,0}+p_{\alpha,1})u_\alpha+\frac{1}{2}(\rho_{\alpha,0}+\rho_{\alpha,1})u_\alpha^3\right]=0\\
&\quad\Rightarrow\ \frac{\partial p_{\alpha,1}}{\partial t}+\gamma p_{\alpha,0}\frac{\partial u_\alpha}{\partial z}=0\ \Rightarrow\ \frac{\partial p_{\alpha,1}}{\partial t}-\frac{\gamma p_{\alpha,0}}{\rho_{\alpha,0}}\frac{\partial \rho_{\alpha,1}}{\partial t}=0\ \Rightarrow\ \frac{\partial p_{\alpha,1}}{\partial t}-c_{\alpha,0}^2\frac{\partial \rho_{\alpha,1}}{\partial t}=0
\end{aligned}\tag{4.5}$$

where in the second step we make use of (4.3). We introduce $c_{\alpha,0}=\sqrt{\frac{\gamma p_{\alpha,0}}{\rho_{\alpha,0}}}$ as the sound velocity of each specie.

As a summary, we show the linearized set of equations:

$$\frac{\partial \rho_{n,1}}{\partial t}+\rho_{n,0}\frac{\partial u_n}{\partial t}=0 \tag{4.6}$$

$$\frac{\partial \rho_{c,1}}{\partial t}+\rho_{c,0}\frac{\partial u_c}{\partial t}=0 \tag{4.7}$$

$$\rho_{n,0}\frac{\partial u_n}{\partial t}+\frac{\partial p_{n,1}}{\partial z}=-\alpha_0\rho_{n,0}\rho_{c,0}(u_n-u_c) \tag{4.8}$$

$$\rho_{c,0}\frac{\partial u_c}{\partial t}+\frac{\partial p_{c,1}}{\partial z}=\alpha_0\rho_{n,0}\rho_{c,0}(u_n-u_c) \tag{4.9}$$

$$\frac{\partial p_{n,1}}{\partial t}-c_{n,0}^2\frac{\partial \rho_{n,1}}{\partial t}=0 \tag{4.10}$$

$$\frac{\partial p_{c,1}}{\partial t}-c_{c,0}^2\frac{\partial \rho_{c,1}}{\partial t}=0 \tag{4.11}$$

where we explicitly write the expression of the drift velocity for future proposes.

Now, we are interested in obtaining a set of two equations that only depends on one of the perturbed fields. The process is analogue to single-fluid calculations but, in this case, collisional terms couple the perturbed fields of the species and we have to deal with a set of wave equations instead of one wave equation.

We choose the velocity field for the following steps. We take partial time derivatives on (4.8) and (4.9):

$$\rho_{\alpha,0}\frac{\partial^2 u_\alpha}{\partial t^2}+\frac{\partial}{\partial z}\left(\frac{\partial p_{\alpha,1}}{\partial t}\right)=-\varepsilon_\alpha\alpha_0\rho_{n0}\rho_{c,0}\left(\frac{\partial u_n}{\partial t}-\frac{\partial u_c}{\partial t}\right) \tag{4.12}$$

The set of equations is obtained from (4.12) by substituting (4.10) and (4.11):

$$\begin{cases}
\rho_{n,0}\frac{\partial^2 u_n}{\partial t^2}-c_{n,0}^2\rho_{n,0}\frac{\partial^2 u_n}{\partial z^2}=-\alpha_0\rho_{n,0}\rho_{c,0}\left(\frac{\partial u_n}{\partial t}-\frac{\partial u_c}{\partial t}\right)\\
\rho_{c,0}\frac{\partial^2 u_c}{\partial t^2}-c_{c,0}^2\rho_{c,0}\frac{\partial^2 u_c}{\partial z^2}\ \ =\ \ \alpha_0\rho_{n,0}\rho_{c,0}\left(\frac{\partial u_n}{\partial t}-\frac{\partial u_c}{\partial t}\right)
\end{cases}\tag{4.13}$$

The coefficients of the equations above are constant so, as in the case of single-fluid, a monocromatic wave solution can be proposed. In a medium with high collisions, such as the solar photosphere, the transmission of momentum and energy between neutrals and charges is very efficient. Under these considerations, it is reasonable to assume that the wavenumbers of both species are the same. This assumption will be discussed late. Then, we can propose the following solutions to (4.13):

$$\{u_n,u_c,\rho_{n,1},\rho_{c,1},p_{n,1},p_{c,1}\}=\{U_n,U_c,R_n,R_c,P_n,P_c\}e^{i(kz-\omega t)} \tag{4.14}$$

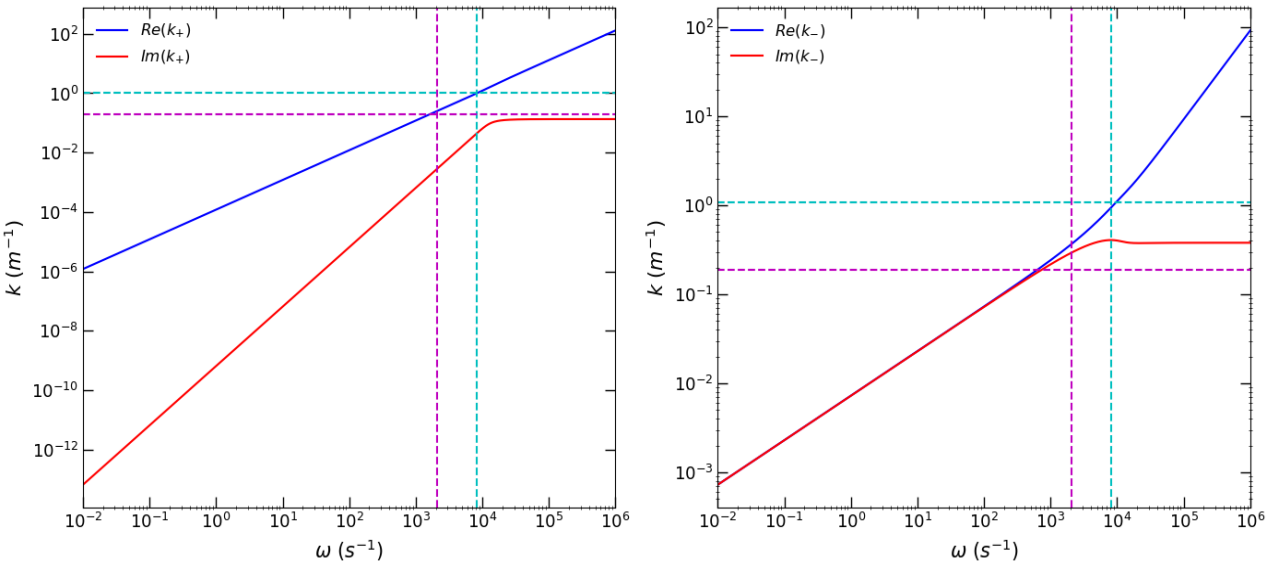

Figure 4.1: Positive solutions of the dispersion equation (4.18). The real and imaginary part of each one are represented. The collisional frequencies and their associated wavenumbers represented by dashed lines (cyan for neutrals and magenta for charges) show the transition region from the 'growing up' dispersion region to the saturated dispersion region.

The applicability of this approach will be discussed later.

After substituting (4.14) in (4.13), we obtain the following set of equations:

$$\begin{cases} (-\rho_{n,0}\omega^2 + c_{n,0}^2\rho_{n,0}k^2 - i\omega\alpha_0\rho_{n,0}\rho_{c,0})U_n + & i\omega\alpha_0\rho_{n,0}\rho_{c,0}U_c = 0 \\ i\omega\alpha_0\rho_{n,0}\rho_{c,0}U_n + (-\rho_{c,0}\omega^2 + c_{c,0}^2\rho_{c,0}k^2 - i\omega\alpha_0\rho_{n,0}\rho_{c,0})U_c = 0 \end{cases} \tag{4.15}$$

This is a homogeneous system of equations. Since we are not interested in the trivial solution, the system must fulfil that its associated determinant is null. This condition leads to the following dispersion relation:

$$i\omega^4 - \alpha_0(\rho_{n,0} + \rho_{c,0})\omega^3 - ik^2(c_{n,0}^2 + c_c^2)\omega^2 + k^2\alpha_0(\rho_{n,0}c_{n,0}^2 + \rho_{c,0}c_{c,0}^2)\omega + ik^4c_{n,0}^2c_{c,0}^2 = 0 \tag{4.16}$$

which is similar to the expression 4.5 obtained in Popescu Braileanu (2020). In our study, we will rewrite it as

$$k^4 - \left[\left(\frac{1}{c_{n,0}^2} + \frac{1}{c_{c,0}^2}\right)\omega^2 + i\alpha_0\left(\frac{\rho_{c,0}}{c_{n,0}^2} + \frac{\rho_{n,0}}{c_{c,0}^2}\right)\omega\right]k^2 + \frac{\omega^3}{c_{n,0}^2c_{c,0}^2}[\omega + i\alpha_0(\rho_{n,0} + \rho_{c,0})] = 0 \tag{4.17}$$

a biquadratic equation in k, whose solutions are:

$$k_{\pm,\pm} = \pm\sqrt{-\frac{B}{2} \pm \sqrt{\frac{B^2}{4} - C}} \tag{4.18}$$

with $A = 1, B, C$ the coefficients of (4.17).

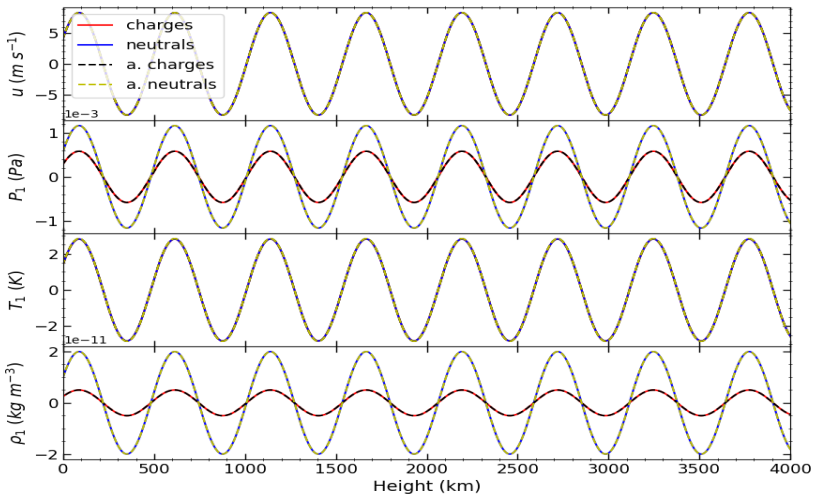

Figure 4.2: Comparison between numerical (solid lines) and analytic solutions (dashed lines) for the homogeneous atmosphere 4.1 with $\omega = 0.1\ s^{-1}$. The perturbation is generated at the bottom.

The expressions for the amplitude coefficients of (4.14) are:

$$\begin{aligned} U_n &= \frac{\omega R_n}{k\rho_{n,0}}; \qquad U_c = \frac{\omega R_c}{k\rho_{c,0}} \\ P_n &= c_{n,0}^2 R_n; \qquad P_c = c_{c,0}^2 R_c \\ \frac{R_n}{R_c} &= \frac{\alpha_0 \rho_{n,0}\omega}{ik^2 c_{n,0}^2 - i\omega^2 + \alpha_0 \rho_{c,0}\omega} \end{aligned} \tag{4.19}$$

which are obtained by substituting (4.14), in the linearized set of equations.

One of the coefficients must be known to determine the rest. In our configuration, we define $R_c = A_c \rho_{c,0}$, with $A_c = 10^{-3}$. At this point, it is interesting to raise the following discussion. Let us consider too that $R_n = A_n \rho_{n,0}$. Then,

$$A_n = \frac{\alpha_0}{-i\frac{\omega^2 - k^2 c_{n,0}^2}{\omega \rho_{c,0}} + \alpha_0} A_c \tag{4.20}$$

If the collisional parameter is large enough, $A_n \approx A_c$ and the result is in concordance with the perturbative scheme. It is important to note that we are in conditions to apply the single-fluid model, so $c_{n,0} \approx c_{s,0}$ and $\omega^2 - k^2 c_{n,0}^2 \approx 0$ since this expression corresponds to the single-fluid dispersion relation. Otherwise, the modulus of the denominator is greater than the numerator, so there are no restrictions in the applicability of the solution. Note that, if we had chosen A_n as a free parameter, the small perturbative approach would not be satisfied in some situations since $|A_c| \geq |A_n|$. Therefore, choosing A_c as a free parameter makes our configuration robust.

To close the discussion, let us review the assumption of $k_n = k_c = k$. Let as denote $\Delta k = k_n - k_c$ and $k = k_c$, so $k_n = k + \Delta k$. In this approach, we must consider that $\omega_n \neq \omega_c$. We will apply the same construction to temporal frequencies as spatial ones. This way, we obtain from (4.13):

$$\begin{cases} (-\rho_{n,0}\omega^2 + c_{n,0}^2 \rho_{n,0} k^2 - i\omega\alpha_0 \rho_{n,0}\rho_{c,0})U_n + & i\omega\alpha_0 \rho_{n,0}\rho_{c,0} e^{-i(\Delta k z - \Delta w t)} U_c = 0 \\ i\omega\alpha_0 \rho_{n,0}\rho_{c,0} e^{i(\Delta k z - \Delta w t)} U_n + (-\rho_{c,0}\omega^2 + c_{c,0}^2 \rho_{c,0} k^2 - i\omega\alpha_0 \rho_{n,0}\rho_{c,0})U_c = 0 \end{cases} \tag{4.21}$$

It is easy to prove that we obtain the same dispersion relation. Since (4.21) must be satisfied at any time and altitude, there is only one possibility: $\Delta k = \Delta\omega = 0$, i.e., the solution proposed as solution before. Otherwise, $\Delta k = \Delta k(z,t)$ and $\Delta\omega = \Delta\omega(z,t)$, and (4.21) is not valid. As conclusion, if $k_n \neq k_c$, they cannot be constants. As our equilibrium state is homogeneous and stationary, this solution can only be obtained from special boundary conditions, which are not of interest to the study.

Let us propose the configuration described in 4.1. We start studying the solutions of the dispersion equation (4.17). We are interested in solutions where the wave propagates from the bottom to the top, i.e., $\mathrm{Re}(k_{\pm,\pm}) > 0$, since this is the criterion that we will follow to generate the perturbations. This is the case of $k_{+,\pm}$ solutions (see Fig. 4.1). We distinguish three regions: the 'growing up' dispersion region, the transition region and the saturated dispersion region. When the frequency of the perturbation is much smaller than the collisional frequencies, we are in the first case. For k_+[1], $\mathrm{Re}(k_+) \gg \mathrm{Im}(k_+)$, and the damping of this mode is extremely weak in distances of the order of the wavelength or even more orders for very low frequencies. This mode is commonly denoted as the propagating mode. In the case of k_-, $\mathrm{Re}(k_-) \approx \mathrm{Im}(k_-)$, the damping scale is approximately the wavelength of the perturbation and it vanishes in short distances. This is known as the non-propagating mode. As shown in Fig. 4.1, propagating and non-propagating modes have very different scales, being the former the ones with the largest wavelength. For frequencies of the order of the collisional frequency, we find the transition region. The real part of the spatial frequency increases its growth and the imaginary part changes significantly its behaviour to enter to a quasi-null growth region for both modes. For frequencies much larger than the collisional frequency, the real part of k continues its growth while the imaginary part seems to tend to a constant value. In this situation, the mean free path of neutrals and charges is larger than the wavelength of the perturbation and the single-fluid approximation is not appropriate, so the solution obtained might not be physically correct.

Now, we present the result of the numerical experiment. At the beginning of the work, the author compiled the code Mancha3D-2F and ran the most basic simulations from the sample tests: the evolution of a monochromatic wave in a homogeneous atmosphere. In this case, the wave is defined analytically in all the points of the domain at the initial time. The first simulation that we configured was the propagation of a monochromatic wave in a homogeneous atmosphere (see Fig. 4.1). In contrast with the previous case, the atmosphere is in equilibrium at the initial time and then a perturbation starts its propagation along the medium. The perturbation is generated via a driver: in the additional cells outside of the physical domain (the ghost cells), at the bottom of the atmosphere, the perturbation is evaluated continuously from the analytical model. In most cases, the number of ghost shells used is three. When this perturbation gets inside the physical domain, the numerical scheme of the code evaluates the numerical solution.

4.2.1 Acoustic waves in the solar atmosphere

The homogeneous plasma model gives us an idea about the behaviour of the system in a very small area. If we want to study the propagation of waves along the vertical axis of the atmosphere, we need to introduce the solar gravity, $g_\odot$, which leads to a stratification of the equilibrium fields.

As in the previous case, we configure analytically the driver and then we study its evolution along the atmosphere. We use a numerical model from Vernazza et al. (1981), the C model, as the background configuration (see Fig. 4.3), so some approximations must be done in the analytic derivation of the driver expressions. At the bottom of the atmosphere, the conditions are similar to the solar photosphere and the single-fluid model can be applied. Then, we will have to obtain the expressions for neutrals and charges from the single-fluid solution. Another simplification is to consider an isothermal atmosphere. This approach is reasonable since, in the region where the driver is applied, the temperature is practically constant. Considering the same simplifications as in the homogeneous

[1]From now, we take the more compact notation $k_{+,\pm} = k_\pm$.

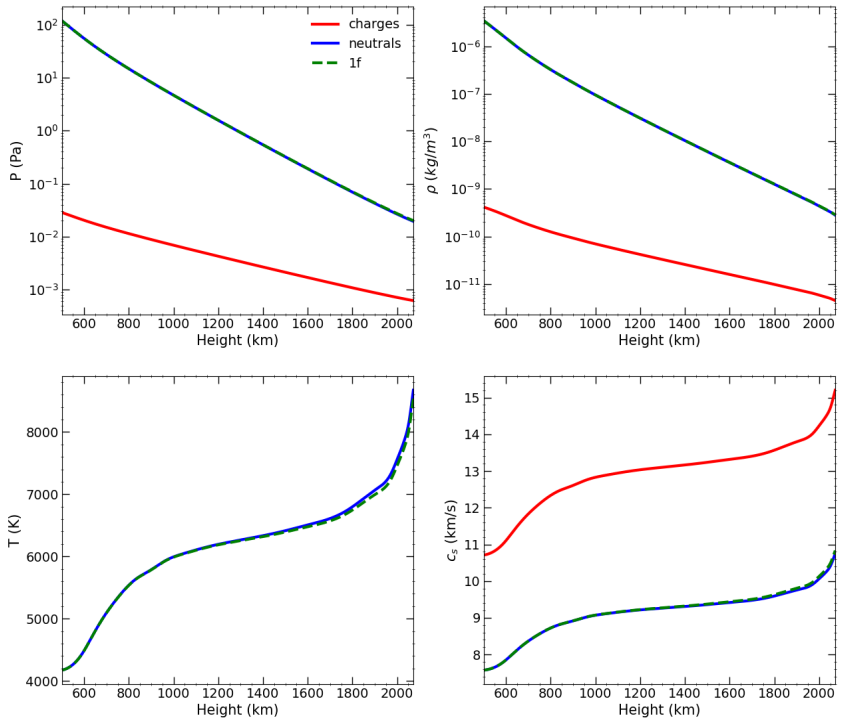

Figure 4.3: Characterization of the VAL-C model for single-fluid and two-fluid configurations. The bottom of the atmosphere is set to 500 km to have a rich background of free electrons so that the electrons come from Hydrogen instead of other elements, such as in deeper layers

case, we derive from (3.45), (3.46) and (3.47) the background conditions:

$$\frac{\partial \rho_0}{\partial t} = 0; \qquad \frac{\partial p_0}{\partial t} = 0; \qquad \frac{dp_0}{dz} = -\rho_0 g_\odot \tag{4.22}$$

where we use the total derivative in the last equation since the partial time derivative of the pressure and density are null.

From the ideal gas law, we can write the density as a function of the pressure. Therefore, the equilibrium pressure is,

$$p_0(z) = p_0(0) e^{-\frac{z}{H}}; \qquad H = \frac{k_B T}{\mu m_n g_\odot} = \frac{p_0}{\rho_0 g} = \frac{c_s^2}{\gamma g} \tag{4.23}$$

where H is the pressure scale.

Now, we obtain the linearized momentum equations. For the mass conservation,

$$\frac{\partial(\rho_0 + \rho_1)}{\partial t} + \frac{\partial[(\rho_0 + \rho_1)u]}{\partial z} = 0 \;\Rightarrow\; \frac{\partial \rho_1}{\partial t} + \rho_0 \frac{\partial u}{\partial z} - \frac{\rho_0}{H} u = 0 \tag{4.24}$$

For the momentum conservation,

$$\begin{gathered}\frac{\partial[(\rho_0+\rho_1)u]}{\partial t}+\frac{\partial[(\rho_0+\rho_1)u^2+(p_0+p_1)]}{\partial z}=-(\rho_0+\rho_1)g_\odot \\ \Rightarrow\ \rho_0\frac{\partial u}{\partial t}+\frac{\partial p_1}{\partial z}+\frac{\partial p_0}{\partial z}=-\rho_0 g_\odot-\rho_1 g_\odot\ \Rightarrow\ \rho_0\frac{\partial u}{\partial t}+\frac{\partial p_1}{\partial z}=-\rho_1 g_\odot\end{gathered} \tag{4.25}$$

And the energy conservation,

$$\begin{gathered}\frac{\partial}{\partial t}\left[\frac{1}{\gamma-1}(p_0+p_1)+\frac{1}{2}(\rho_0+\rho_1)u^2\right]+\frac{\partial}{\partial z}\left[\frac{\gamma}{\gamma-1}(p_0+p_1)u+\frac{1}{2}(\rho_0+\rho_1)u^3\right]=-(\rho_0+\rho_1)ug_\odot \\ \Rightarrow\ \frac{1}{\gamma-1}\frac{\partial p_1}{\partial t}+\frac{\gamma}{\gamma-1}\frac{\partial(p_0u)}{\partial z}=-\rho_0 gu\ \Rightarrow\ \frac{\partial p_1}{\partial t}+\gamma p_0\frac{\partial u}{\partial z}=\rho_0 g_\odot u\ \Rightarrow\ \frac{\partial p_1}{\partial t}-c_{s,0}^2\frac{\partial \rho_1}{\partial t}=-(\gamma-1)\rho_0 g_\odot u\end{gathered} \tag{4.26}$$

where we made use of (4.23) and (4.24).

As summary, we show the set of momentum equations:

$$\frac{\partial \rho_1}{\partial t}+\rho_0\frac{\partial u}{\partial z}-\frac{\rho_0}{H}u=0 \tag{4.27}$$

$$\rho_0\frac{\partial u}{\partial t}+\frac{\partial p_1}{\partial z}=-\rho_1 g_\odot \tag{4.28}$$

$$\frac{\partial p_1}{\partial t}-c_{s,0}^2\frac{\partial \rho_1}{\partial t}=-(\gamma-1)\rho_0 g_\odot u \tag{4.29}$$

We take partial time derivatives over (4.28):

$$\rho_0\frac{\partial^2 u}{\partial t^2}+\frac{\partial}{\partial z}\left(\frac{\partial p_1}{\partial t}\right)=-\frac{\partial \rho_1}{\partial t}g_\odot \tag{4.30}$$

Then, we make use of (4.29):

$$\rho_0\frac{\partial^2 u}{\partial t^2}+\frac{\partial}{\partial z}\left(c_{s,0}^2\frac{\partial \rho_1}{\partial t}-(\gamma-1)\rho_0 g_\odot u\right)=-\frac{\partial \rho_1}{\partial t}g_\odot \tag{4.31}$$

If we introduce (4.27) in (4.31) and develop the results, we finally obtain the wave equation for a stratified isothermal atmosphere:

$$\frac{\partial^2 u}{\partial t^2}=c_{s,0}^2\frac{\partial^2 u}{\partial z^2}-\gamma g_\odot\frac{\partial u}{\partial z} \tag{4.32}$$

The coefficients of the equation above are constant, and a monocromatic wave solution can be proposed. In contrast with the homogeneous case, we have to choose carefully the definition of the coefficients as follows:

$$\left\{\frac{u}{c_s},\frac{\rho_1}{\rho_0},\frac{p_1}{p_0}\right\}=\{\tilde{V},\tilde{R},\tilde{P}\}e^{i(kz-\omega t)} \tag{4.33}$$

this way, we ensure that the coefficients are constants and that the development is consistent.

The dispersion relation is obtained applying this solution to (4.32):

$$\omega^2=c_{s,0}^2k^2+i\gamma g_\odot k \tag{4.34}$$

If we fix the temporal frequency, the spatial frequency is given by:

$$k_{\pm} = \frac{\omega_{cut}}{c_s}\left[-i \pm \sqrt{\left(\frac{\omega}{\omega_{cut}}\right)^2 - 1}\right]; \qquad \omega_{cut} = \frac{\gamma g_{\odot}}{2c_s} \tag{4.35}$$

with ω_{cut} the cutoff frequency of the stratified isothermal atmosphere.

We impose in our solution that $u_n = u_c = u$ and fix $\tilde{V} = 10^{-3}$. From the continuity equation (4.27):

$$-i\omega\rho_0\tilde{R} + ik\rho_0 c_s\tilde{V} - \frac{\rho_0}{H}c_s\tilde{V} = 0 \;\Rightarrow\; \tilde{R} = (i + Hk)\frac{c_s}{\omega H}\tilde{V} \tag{4.36}$$

The coefficient of the pressure is obtained from the momentum conservation equation (4.28):

$$i\frac{\omega p_0 c_s}{Hg}\tilde{V} = ikp_0\tilde{P} - \frac{p_0}{H}\tilde{P} + \frac{p_0}{H}\tilde{R} \;\Rightarrow\; \tilde{P} = \frac{\tilde{R} - i\frac{\omega c_s}{g}\tilde{V}}{1 - iHk} \;\Rightarrow\; \tilde{P} = \frac{\frac{kc_s}{\omega} + i\left(\frac{c_s}{\omega H} - \frac{\omega c_s}{g}\right)}{1 - iHk}\tilde{V} \tag{4.37}$$

At this point, we can configure the amplitude of the perturbations for both species as follows:

$$\begin{aligned} V_n &= V_c = c_s\tilde{V} \\ R_n &= \frac{\rho_n}{\rho}\tilde{R}; \quad R_c = \frac{\rho_c}{\rho}\tilde{R} \\ P_n &= \frac{p_n}{p}\tilde{P}; \quad P_c = \frac{p_c}{p}\tilde{P} \end{aligned} \tag{4.38}$$

The dispersion equation solution (4.35) and the set of coefficients (4.38) provide the expressions to configure the initial perturbation in the stratified atmosphere in absence of magnetic field.

4.2.2 An analytical approximation to the single-fluid solution

The first step in the study of the two-fluid acoustic waves in a stratified atmosphere is to check that the solution obtained in single-fluid conditions (low frequencies) agrees with the single-fluid solution. In addition, the single-fluid numerical solution must also be checked with an analytical solution to enhance the confidence in the comparison. As indicated above, the use of a numerical model for the background atmosphere introduces a limitation in the analytical results that can be obtained. We propose the following analytical description: let us divide the whole atmosphere in small layers of constant temperature, each one with the same thickness Δz. In each layer, the isothermal solution is valid, so that we can make a local description of the perturbation applying (4.35), (4.36) and (4.37). Unlike the amplitude coefficients, the phase of the perturbation depends on the layers that has gone through. At the end of the first layer, the phase will be $\phi_0 = k_0\Delta z$; at the end of the second one, we will find $\phi_1 = (k_0 + k_1)\Delta z$. Then, on the M-th layer $\phi_m = \sum_{m=0}^{M-1} k_m\Delta z$. The limit $\Delta z \to 0$ leads to the integral expression:

$$\phi(z) = \int_0^z k(z')dz' \tag{4.39}$$

It is important to note that this is a zero-th order approximation, i.e., we are considering that the gradients between layers are negligible. According to Fig. 4.3, this simplification seems reasonable.

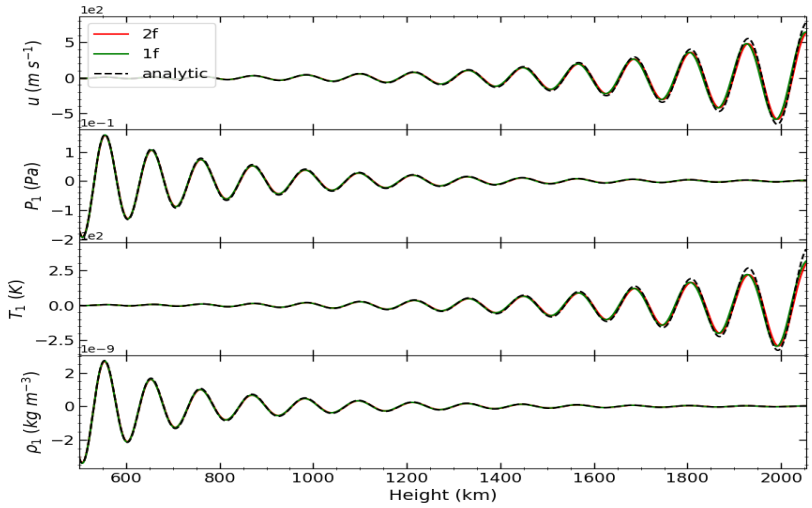

Figure 4.4: Comparison between the single-fluid solution (green line) with the two-fluid solution (red line) calculated using (4.40) for a perturbation with $\omega = 0.5\ s^{-1}$. Black dashed line shows the analytical solution.

The earliest test results are shown in Fig. 4.4. The two-fluid solutions represented are:

$$\begin{aligned} v_{2f} &= \frac{\rho_n u_n + \rho_c u_c}{\rho_n + \rho_c} \\ p_{2f} &= p_n + p_c \\ T_{2f} &= \frac{\rho_n T_n + \rho_c T_c}{\rho_n + \rho_c} \\ \rho_{2f} &= \rho_n + \rho_c \end{aligned} \tag{4.40}$$

which are the thermodynamical fields measured in the center of mass of both species. When we consider the case of low frequencies, the three solutions are practically the same. Some differences appear in the highest layers of the atmosphere. On one side, the amplitude of the analytic solution (black dashed line) is larger than the single-fluid numerical solution (green line), which suggests that our theoretical approach is not accurate enough in this region. This is due to the fact that the temperature gradient is very strong in the upper part of our atmosphere. On the other, we observe that the phases of the single-fluid and two-fluid solutions are slightly different due to the different sound velocity of both species. Since we include electrons in the state equation of the charges, the same temperature for both species does not mean that their sound velocity are equal.

The representation of the two-fluid solutions in a space-time diagram allows us a deeper understanding in the particular behaviour of neutrals and charges (see Fig. 4.5) Velocity and temperature perturbations are quite similar. This is evident from the fact that pairs of images at the first and the third row of panels are indistinguishable by eye. Perturbations in pressure and density for neutrals show a strong attenuation (left panels in the second and firth row). This behaviour is as predicted by the single-fluid solution. Such an attenuation with height cannot be appreciated for the charges. At first sight, the result is shocking because the perturbation in temperature is the same for both species. However, one must keep in mind the following aspects: the perturbation in temperature is not related

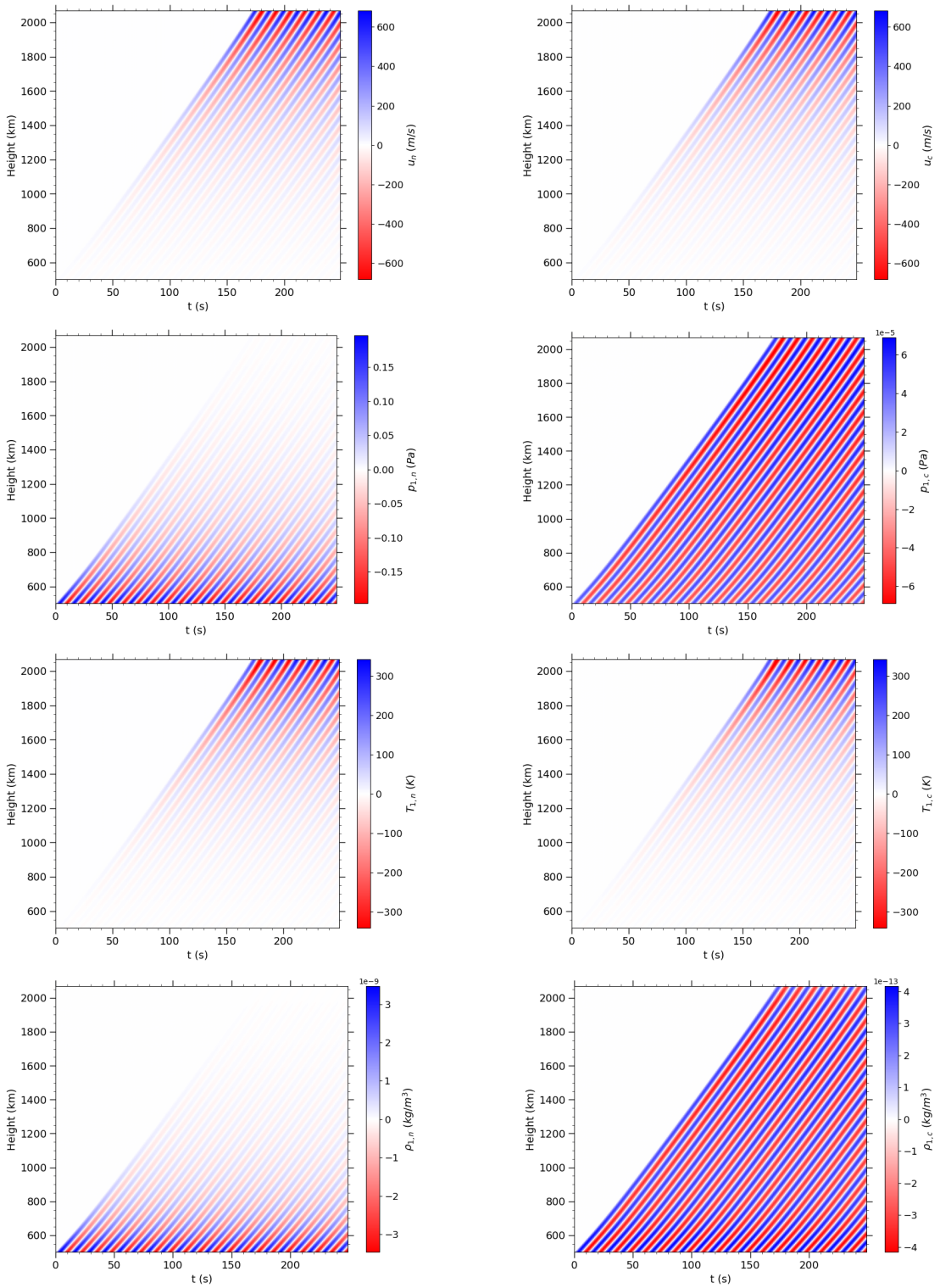

Figure 4.5: Space-time diagram for the thermodynamic fields for neutrals (left) and charges (right).

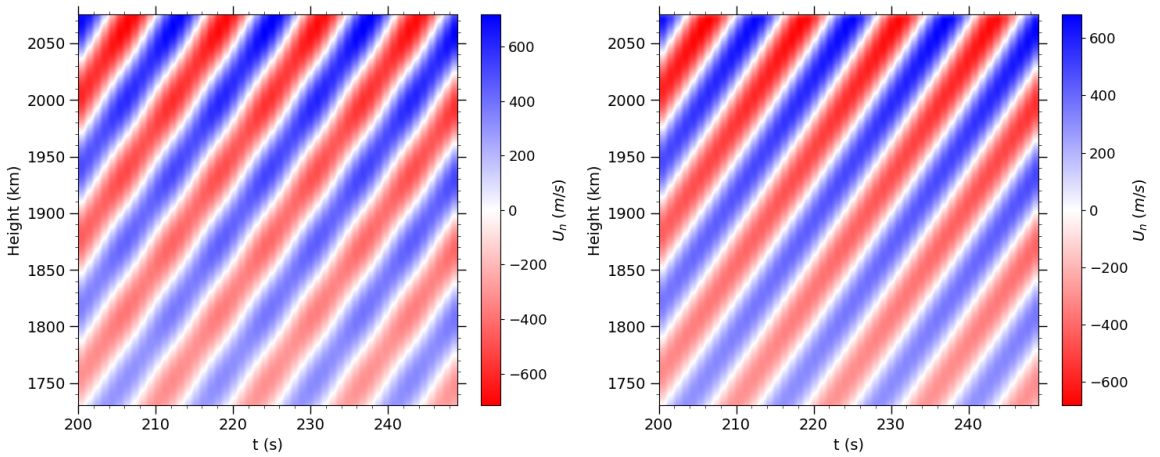

Figure 4.6: On the left, the time-space diagram of a perturbation whose PML condition is bad adjusted. On the right, the pml condition is adjusted properly. In the first case, the profile of the bands show oscillations after the perturbation reaches the top of the atmosphere. This effect indicates the presence of reflections produced by the boundary conditions.

with the ratio of pressure and density perturbations, but it is computed as:

$$T_{\alpha,1} = \frac{\mu_\alpha m_n}{k_B}\left(\frac{p_\alpha}{\rho_\alpha} - \frac{p_{\alpha,0}}{\rho_{\alpha,0}}\right) \tag{4.41}$$

This explains why oscillations of temperature in both species are so similar. It has to be noted that the pressure scale for charges is a factor 2 greater than for the neutrals. Therefore, the decrease of the density with height is much less pronounced for charges than for neutrals. Neutrals have larger density in all the layers. If the variations of pressure and density of both species are shown normalized to their corresponding background values, the relative oscillations of all the quantities increase with height, similar to those of the velocity.

Despite the simplicity of the simulation, it shows that the analysis of numerical solutions is not easy. Even when we can make use of an analytical estimation of the solution, the deviations from the numerical solution are not only due to the limitations of the approach. The effects caused by the numerical implementation of the problem must be studied carefully to reduce their contribution and improve the confidence on the solution. In the previous case, it is important to calibrate appropriately the PML layer (see Fig. 4.6) to avoid numerical reflections that propagate along the domain.

Once the code is tested, we configure simulations in a range of frequencies large enough to observe the effects of the collisional terms (see Fig. 4.7). We show the solutions obtained for the perturbation with the highest frequency studied[2] (see Figs. 4.8 and 4.9). These figures compare the numerical two-fluid solution (red lines) with the single fluid solution in the adiabatic approximation (green line) at the upper panels. The bottom panels show a close-up of the solution at a reduced range of heights, one of them at the bottom chromosphere and another one at the upper chromosphere. The difference between these figures is in different collisional cross-sections used, as we explain below. For both two-fluid simulations we observe a damping in the amplitude of the perturbed fields in the highest layers, which the single-fluid model cannot reproduce. This behaviour is caused by the interaction between neutrals and charges, which is not present in the single-fluid description. It is important to remark that the simulations are performed only with linear terms, so we observe a linear damping. Another interesting result is the decoupling of velocities of neutrals and charges in the highest layers of the

[2] An empirical criterion stablishes that a perturbation is well resolved if the density of points per period is larger than 8. Since k grows with ω, higher frequencies impose higher spatial resolution. Then, the computational time grows with ω, introducing a limitation in the range of frequencies that can be studied.

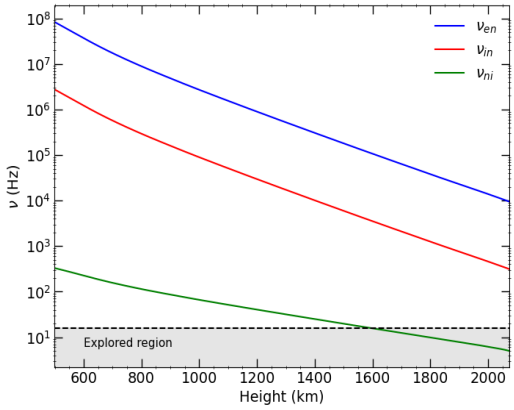

Figure 4.7: Main collisional frequencies of the VAL-C atmosphere considering a plasma composed only by hydrogen. The region of frequencies studied are delimited by the dashed line. The computational time imposes the barrier of or study.

atmosphere. This decoupling can be seen as s difference in the amplitude or phase of the velocities of neutrals and charges at the close-up panels at the bottom of Figs. 4.8 and 4.9. Fig. 4.10 shows the decoupling velocities as a function of height for both simulations. The decoupling increases with height in the atmosphere. This suggests that the relative amplitude and phase between the velocity of the two species is a function of the altitude and that is higher for high frequencies.

Figs. 4.8 and 4.9 shows qualitatively similar results, but the magnitude of the decoupling and wave damping is significantly different. This difference is caused by the use of different cross-sections for the collisions, taken from the works of Leake et al. (2012b) (Fig. 4.9) and Leake et al. (2013) (Fig. 4.8). The change of the one order of magnitude in the effective ion-neutral cross sections involved in the collisional parameter introduced significant differences in the solutions obtained. Since several values for the cross section are discussed in the literature, our result motivates an improvement in the calculus. Nowadays, it is not possible to observe waves of this frequency because they cannot be resolved yet, but in the future they may be used to polish the value.

4.3 Acoustic shock waves

When the amplitude of the perturbations is large enough, the non-linear terms cannot be ignored. Consider, as an example, the propagation of a monochromatic wave in a homogeneous atmosphere. The apex of the positive wing of the perturbation moves with the local velocity $c+v$ and the negative moves with $c-v$. Eventually, the apex of the positive wing will catch up the negative one. This leads to a discontinuity in the physical fields called a shock wave. If the wave amplitude becomes larger than the local sound speed, such waves are called 'strong' shock waves. The discontinuities can also appear when we propagate waves with initially small amplitudes in mediums large enough, by the same reasoning. These are called the 'weak' shock waves and are especially important when we propagate high frequency waves. Under these physical conditions, the system tends to increase its internal energy and, as consequence, its temperature. For this reason, shock waves are an interesting mechanism to explain of the chromospheric heating.

The formation of shock waves introduces several difficulties in the numerical solution. In some steps of the solution calculation, the code makes use of the Fourier space. It is known that discontinuities cannot be well reproduced by the Fourier transform, introducing numerical oscillations in the process. This effect is called the Gibbs phenomenon. To smooth these oscillations, the code introduces hyper-diffusivity coefficients, whose values must be adjusted at each simulation. Another problem appears

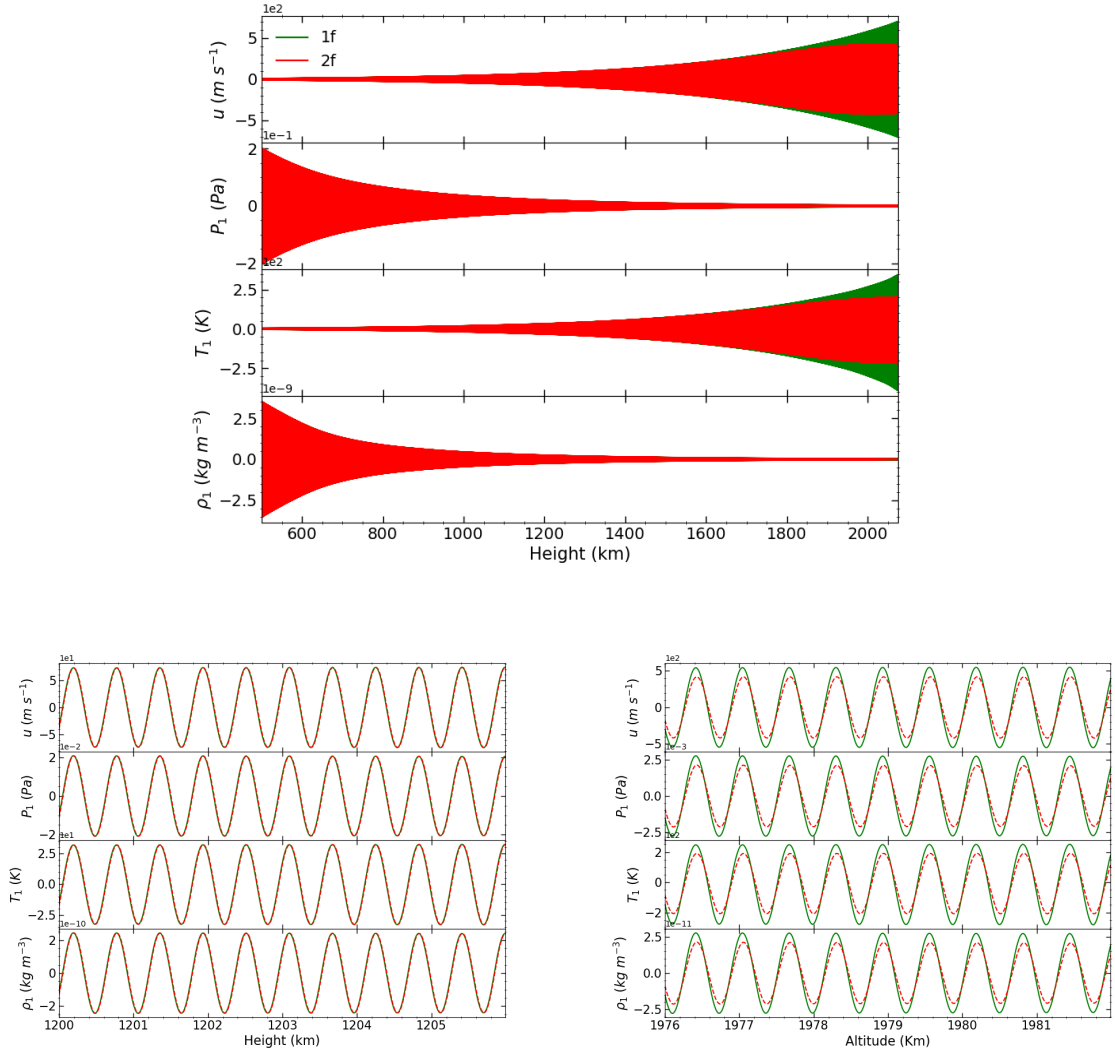

Figure 4.8: Comparison between the two-fluid solution and the single fluid solution for a perturbation with $\omega = 100s^{-1}$ and the effective collisional sections $\sigma_{in} = 1.16 \cdot 10^{-18}\ m^2$ and $\sigma_{en} = 1.0 \cdot 10^{-19}\ m^2$, according to Leake et al. (2013). The figure on the top shows a general view of the profile of each solution. At the bottom, figure on the left zooms a region of the bottom of the atmosphere where both solutions match and the figure on the right zooms a region of the top where differences in phase and amplitude are observed.

when the perturbation enters into the physical domain by the first time. If the initial amplitude is large enough, it can be considered as a discontinuity by the code scheme. To avoid this situation, we introduce a smoothing factor in the analytic perturbation (see Fig. 4.11), such as:

$$f_s(t) = 1 - e^{-t/\tau_s} \tag{4.42}$$

We perform a simulation of a shock wave with $\omega = 10\ s^{-1}$, the highest frequency we explored. Unfortunately, this frequency was not large enough to observe differences between single-fluid and two-fluid solutions, but it is possible to measure the influence of the collisional terms. We show

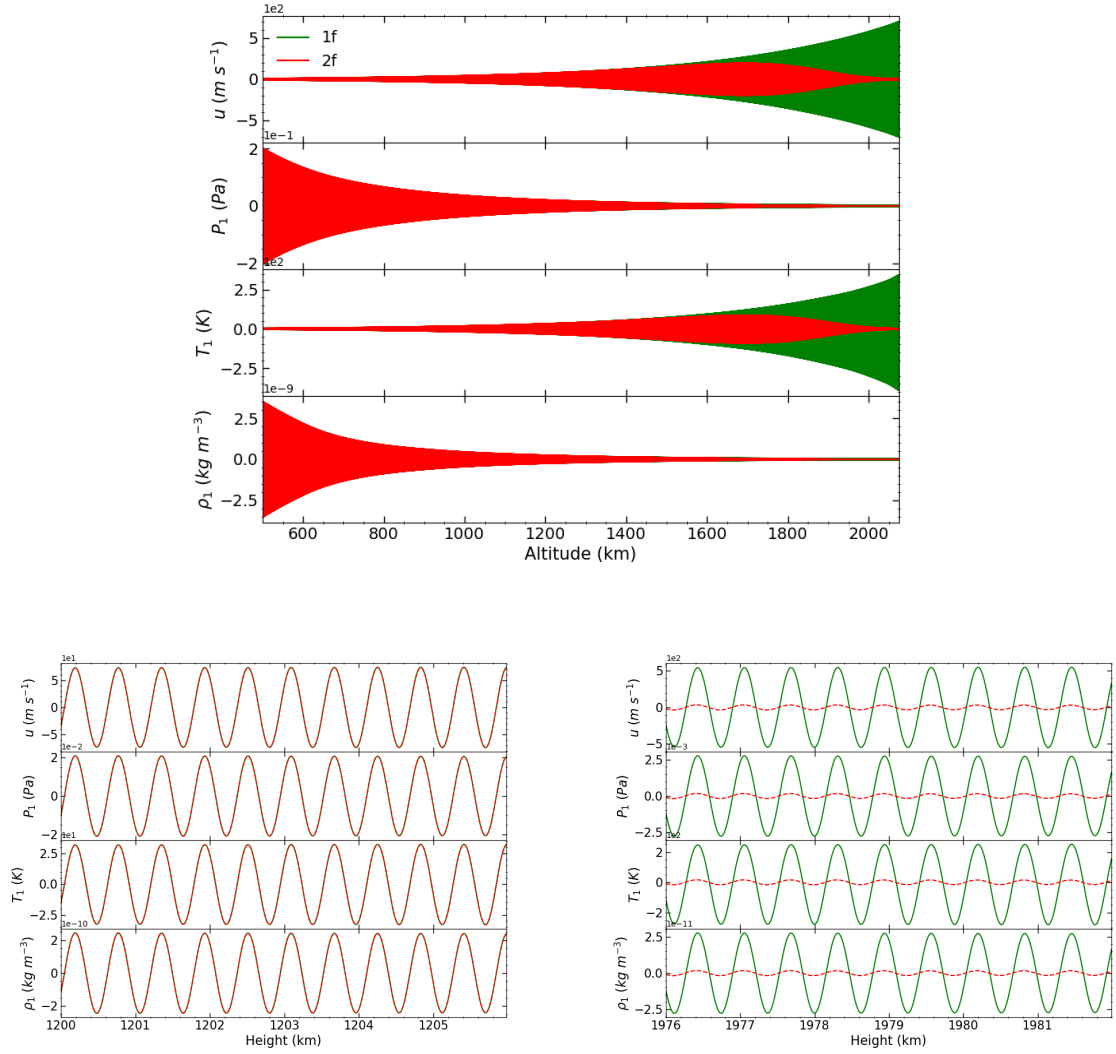

Figure 4.9: Comparison between the two-fluid solution and the single fluid solution for a perturbation with $\omega = 100s^{-1}$ and the effective collisional sections $\sigma_{in} = \sigma_{en} = 1.0 \cdot 10^{-19}\ m^2$, according to Leake et al. (2012b). The figure on the top shows a general view of the profile of each solution. At the bottom, figure on the left zooms a region of the bottom of the atmosphere where both solutions match and the figure on the right zooms a region of the top where differences in phase and amplitude are observed.

the contribution of the terms of the internal energy equation in Fig. 4.12. This figure compares the magnitudes of the energy flux, $\partial u_\alpha e_\alpha / \partial z$ (green lines), of the work of the pressure force, $-P_\alpha \partial u_\alpha / \partial z$ (magenta lines), the thermal exchange (blue lines) and the frictional heating (red lines) contributions to the total internal energy variations in time (yellow lines). For a better visualization we normalized all the contribution to the corresponding background densities. This way, the variations in the upper layers can be appreciated. One can observe that the energy flux is mostly ballanced by the work of the pressure force. In the case of neutrals (left panel) neither thermal exchange nor frictional heating are relevant. On the contrary, for the charges, the thermal exchange contributes most to the time derivative of the internal energy from the half to the top of the atmosphere. This fact indicates that

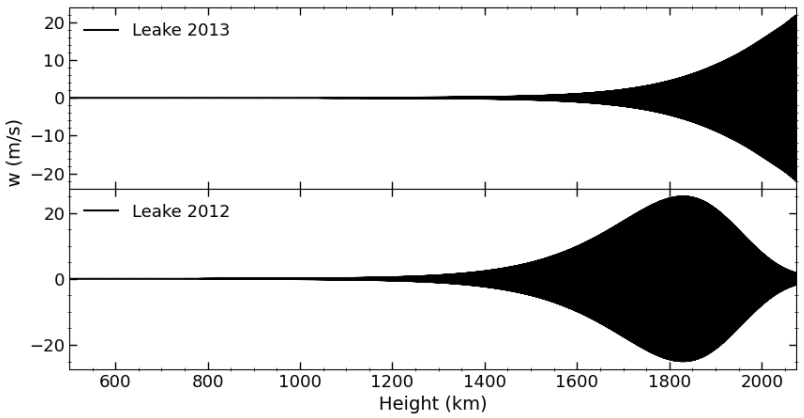

Figure 4.10: Drift velocities, i.e. the difference in the velocities of charges and neutrals for the simulation with $\omega = 100\ s^{-1}$ shown in Figures 4.8 and Fig. 4.9. The difference between the panels are the different collisional cross-sections used.

we are close to the regime where we expect to find differences between the two models.

If we pay attention to the dominant terms, the flux of internal energy and the work of pressure forces, we observe that they reach a maximum (in absolute value) when the shock waves reach its maximum amplitude. At this point, the wave begins to dissipate the energy and the amplitude in velocity and temperature tends to a constant. The density and pressure of the equilibrium atmosphere decrease with altitude, so the amplitudes of the two dominant terms will decrease too. In this representation, the difference in the pressure scale of the species is clear.

As the physical properties of neutrals and charges are the same when we consider only elastic collisions, only small differences between single-fluid and two-fluid predictions are observed. More effects that distinguish the species must be introduced to observe significant differences in the low frequencies regime.

4.4 Magnetoacoustic waves

Our study is focused in the solar chromosphere, where $\beta_{\text{plasma}} < 1$, i.e., the magnetic field dominates the dynamic of the plasma. In the last group of simulations, we introduce a magnetic field oriented along the x-axis. This way, the magnetic field perturbations will be coupled with the acoustic perturbations, giving as result the propagation of magnetoacoustic waves. If we had chosen the direction of the magnetic field along the z-axis, it can be demonstrated that only acoustic waves will propagate along the same direction, which is not an interesting case for our proposes, because these will be exactly the same acoustic waves as the case considered above. When the magnetic field is included, the comparison between single-fluid and two-fluid solutions becomes especially important: the single-fluid model introduces the interaction between neutrals and charges using the ambipolar term. We are introducing an element that distinguishes the species since only charges are affected directly by the electromagnetic field, so we expect more relevant changes in the behaviour of both components.

As in the previous case, some simplifications are made to configure in an easy way the initial perturbation. We generate the perturbation in a region with $\beta_{\text{plasma}} > 1$ and high collisions, so both species are fully coupled and a single-fluid solution can be applied. Additionally, the gas pressure dominates the dynamic of the system and the ambipolar term can be neglected.

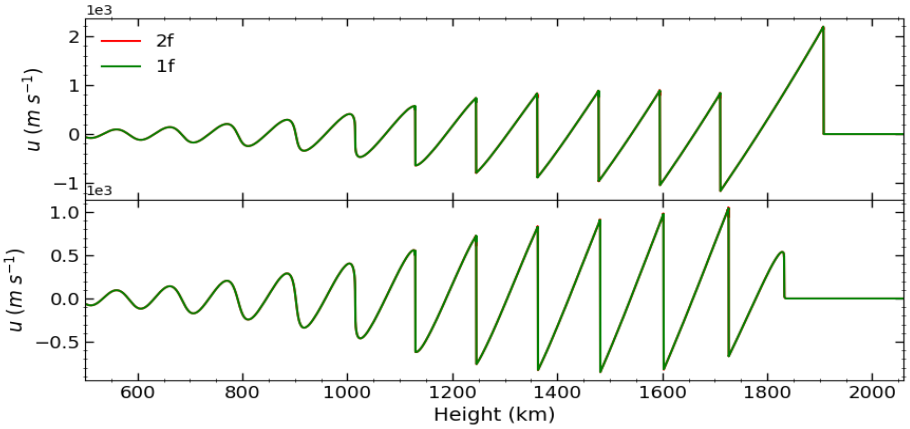

Figure 4.11: Top panel: solution without smoothing factor. Bottom panel: solution with smoothing factor avoids the big pick produced by the introduction of a perturbation of high amplitude.

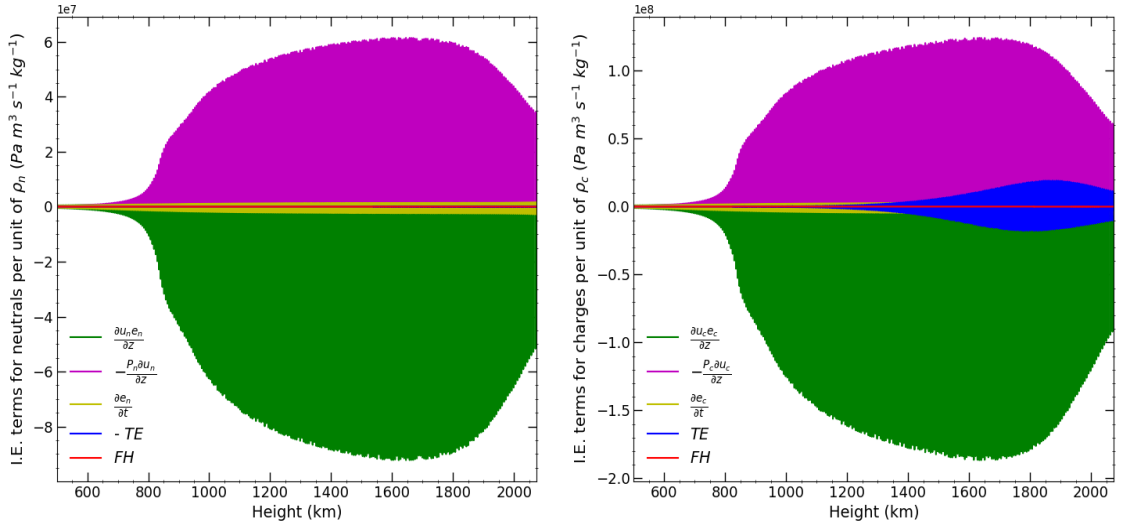

Figure 4.12: Representation of the terms of the internal energy equation for neutrals (left) and charges (right) in a shock wave with $\omega = 10\ s^{-1}$.

Firstly, we configure the equilibrium state. From (3.27) and (3.28), the equilibrium is defined by:

$$\begin{aligned} \frac{\partial p_{n,0}}{\partial z} &= -\rho_{n,0} g_{\odot} \\ \frac{\partial}{\partial z}\left(p_{c,0} + \frac{B_{x,0}^2}{2\mu_0}\right) &= -\rho_{c,0} g_{\odot} \end{aligned} \tag{4.43}$$

which admit a solution with a constant magnetic field. Its value is adjusted by the condition $\beta_{\text{plasma}}(z_{\text{chr}}) = 1$, where z_{chr} is the altitude where the chromosphere starts.

In the region where the perturbation is generated, the single-fluid equilibrium equations are (4.22), as in the case of the pure acoustic waves. The expressions (4.23) are valid too. From (3.48), (3.49)

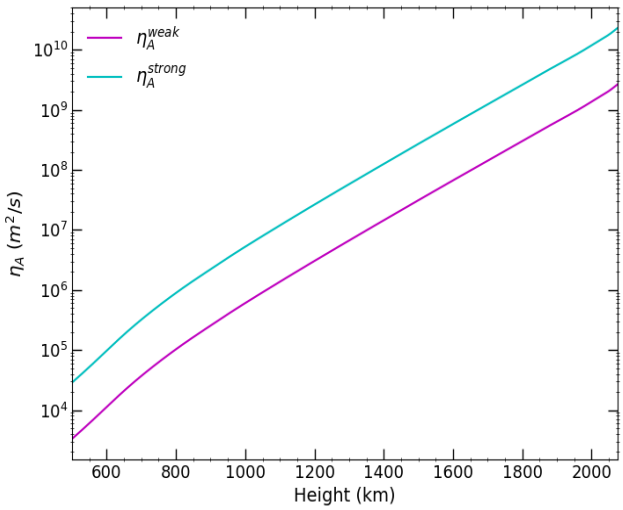

Figure 4.13: Ambipolar diffusivity functions for all the magnetic field configurations tested. The coefficients are obtained using (3.57).

and (3.50), we obtain the linearized set of momentum equations (4.27), (4.29) and for the momentum conservation:

$$\frac{\partial u}{\partial t} + \frac{1}{\rho_0}\frac{\partial p_1}{\partial z} = -\frac{\rho_1}{\rho_0}g_\odot - \frac{1}{\mu_0\rho_0}\left(\frac{\partial B_{x,1}}{\partial z}B_{x,0}\right) \tag{4.44}$$

where we used the Ampère's law (3.22).

Let us obtain the wave equation. We apply a time partial derivative over (4.44) and combine the Ohm's law (3.56) and the induction equation (3.22) to find:

$$\frac{\partial^2 u}{\partial t^2} + \frac{1}{\rho_0}\frac{\partial}{\partial z}\left(\frac{\partial p_1}{\partial t}\right) = -\frac{g_\odot}{\rho_0}\frac{\partial \rho_1}{\partial t} + v_A^2\frac{\partial^2 u}{\partial z^2} \tag{4.45}$$

with $v_A^2 = \frac{B_{x,0}^2}{\mu_0\rho_0}$ the square of the Alfvén velocity. The result is the same as (4.30) plus an additional term, so we directly can write:

$$\frac{\partial^2 u}{\partial t^2} = (c_s^2 + v_A^2)\frac{\partial^2 u}{\partial z^2} - \gamma g_\odot \frac{\partial u}{\partial z} \tag{4.46}$$

Except for the Alfvén velocity, the rest of the coefficients of the wave equation are constant in the isothermal case. The perturbation is generated in a small region and we can safely assume that the Alfvén velocity is uniform and a solution of monochromatic waves to (4.46):

$$\left\{\frac{u}{c_s}, \frac{\rho_1}{\rho_0}, \frac{p_1}{p_0}, \frac{B_{x,1}}{B_{x,0}}\right\} = \{\tilde{V}, \tilde{R}, \tilde{P}, \tilde{B}\}\exp(i(kz - \omega t)) \tag{4.47}$$

obtaining the dispersion relation:

$$\omega^2 = k^2(c_s^2 + v_A^2) + i\gamma g_\odot \tag{4.48}$$

From the continuity equation, the expression for the density amplitude is given by (4.36). From the

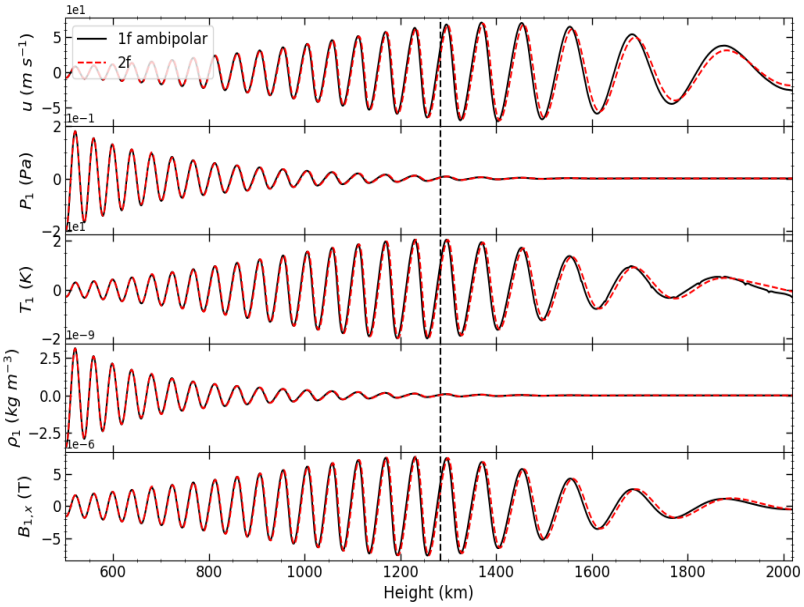

Figure 4.14: Comparison between the two-fluid and single-fluid solutions for a magnetoacoustic wave with $T = 5s$. The transition region ($\beta = 1$) is set at the middle of the atmosphere, shown in vertical black dashed line.

induction equation, we obtain for the magnetic field amplitude:

$$\tilde{B} = \frac{k}{\omega} c_s \tilde{V} \tag{4.49}$$

In the case of the pressure amplitude, from (4.44):

$$\begin{aligned} i\frac{\omega p_0 c_s}{Hg}\tilde{V} = ikp_0\tilde{P} - \frac{p_0}{H}\tilde{P} + \frac{p_0}{H}\tilde{R} + kv_A^2\frac{p_0}{Hg_\odot}\tilde{B} \;\Rightarrow\; i\frac{\omega c_s}{g_\odot}\tilde{V} = iHk\tilde{P} - \tilde{P} + \tilde{R} + iv_A^2\frac{k^2}{g_\odot\omega}c_s\tilde{V} \\ \Rightarrow \tilde{P} = \frac{\frac{kc_s}{\omega} + i\left(\frac{c_s}{\omega H} + v_A^2\frac{k^2}{g_\odot\omega}c_s - \frac{\omega c_s}{g_\odot}\right)}{1 - iHk}\tilde{V} \end{aligned} \tag{4.50}$$

Finally, we use (4.38) to configure the amplitudes for neutrals and charges and the implementation is closed.

We show the numerical results for the cases of 5 s period (see Fig. 4.14) and 1 s period (see Fig. 4.15). The magnetohydrodynamic equations were solved by using all the non-linear terms. These figures compare the single-fluid solution for magneto-acoustic waves with ambipolar term in black line with the two-fluid solution in red dashed line. The solution is shown for the velocity, thermodynamic fields and the horizontal magnetic field component, as a function of height in the chromosphere for a given time moment. This moment is chosen in the stationary regime of the simulations, after the waves reached the upper boundary and several wave trains have passed. In both single-fluid and two-fluid cases we observe an initial wave amplitude increase in velocity and in magnetic field, and a posterior damping. The waves vanish for layers above the middle of the chromosphere. The damping is much more pronounced in the 1 s period case in Fig. 4.15. In the case of the waves of 5 s period, Fig. 4.14, both solutions are quite similar, with small differences in the upper layers of the atmosphere. In the

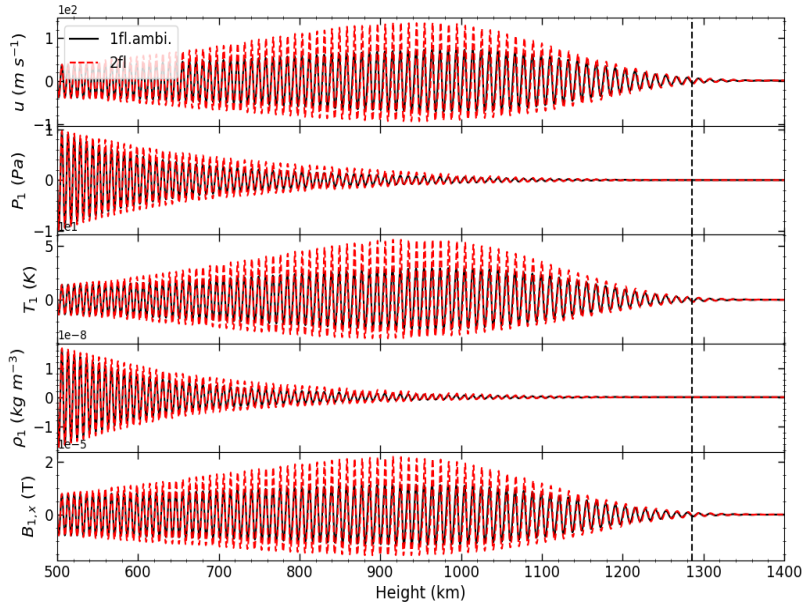

Figure 4.15: Comparison between the two-fluid and single-fluid solutions for a magnetoacoustic wave with $T = 1s$. The transition region ($\beta = 1$) is set at the middle of the atmosphere, shown in vertical black dashed line. Only the low atmosphere is represented because the amplitude of the perturbation is practically null in the highest layers.

second case, Fig. 4.15, the differences are more clear. We observe a different growth in amplitude between two-fluid and single-fluid solutions in the low layers of the chromosphere or the 1 s period case. The amplitude of the two-fluid solution is large enough to show non-linear effects that cannot be seen for the single-fluid solution. Once the perturbation reaches the layer where the damping becomes stronger, the two-fluid solution returns to the linear regime and both solutions tend to the same amplitude. The discussion leads to an important conclusion: for the same physical conditions, the two-fluid solution leads to the formation of shock waves but the single-fluid one does not. The damping introduced by the ambipolar term is more efficient than the explicit neutral-ion collision friction term in the two-fluid description, even in regions dominated by the gas pressure.

The behaviour of the solutions changes significantly in both cases in a small range of periods (1 to 5 s). The possibility of obtaining an analytic solution should give us the keys to understand the nature of the transition. Even in the single-fluid approach, when we do not consider the ambipolar term, obtaining an analytic solution with this configuration is not easy. Following the results presented in the literature, we tried to deduce a solution in terms of hypergeometric functions for the case with ambipolar term, but, unfortunately, the comparison with numerical results was not satisfactory.

The main motivation for the present TFM was the study of a mechanism capable of justifying the chromospheric heating. Attending to the energy collisional terms (3.46) and (3.46), when we introduce an element that distinguishes between neutrals and charges like the magnetic field, the contribution of the Q_c and Q_c terms becomes more relevant, introducing an increment in the internal energy. If the coupling between neutrals and charges is strong enough, the contribution of the thermal exchange term will be negligible and the heating will be the same for both species. We show in Fig. 4.16 the average of the temperature perturbation for several wave periods. The result obtained is clear: the single fluid model predicts a weak heating in regions dominated by the magnetic field, whilst the two-fluid heating is stronger. Both increments in temperature seem to grow with time, being more apparent in

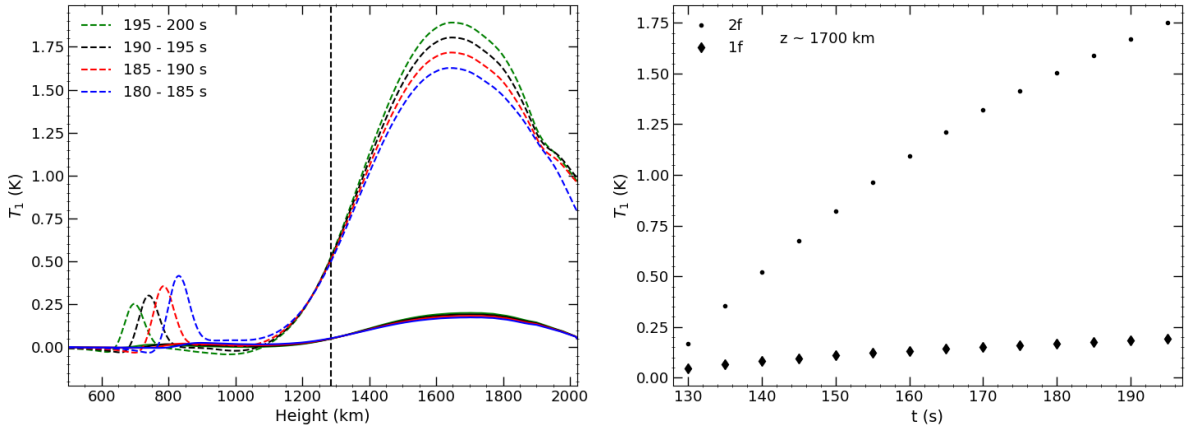

Figure 4.16: Left panel: representation of the time-average temperature perturbation for a two-fluid model (dashed lines) and single-fluid model (solid lines) or the wave period of 5 s. Blue curves are from early times and the green ones for the latest. Right panel: the time evolution of the average temperature perturbation at a fixed height with an maximum heating effect (1700 km).

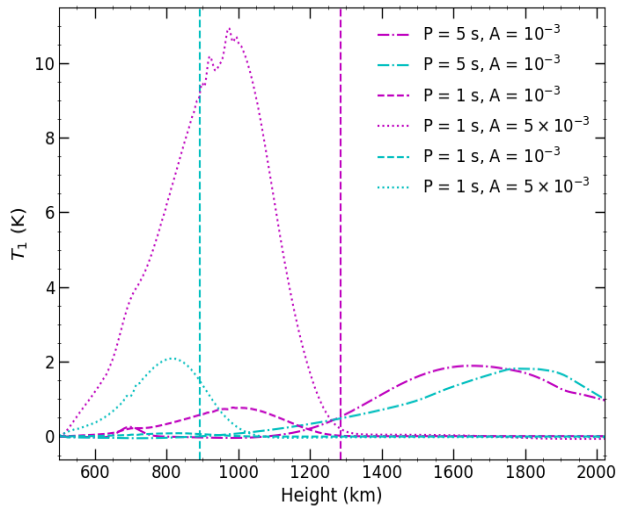

Figure 4.17: Representation of the time-average temperature perturbation for a two-fluid model for different amplitudes of the initial perturbation and wave periods. In magenta, we show the results for a weak field and in cyan, for the strong field.

the two-fluid case. Regarding the additional small peaks observed in the spatial representation of the two-fluid solution at low heights around 800 km, they are most likely the results of numerical effects. Adjusting the boundary conditions when more elements are introduced in the equations becomes more difficult, especially in the two-fluid case.

We summarise the heating results for different configurations in Fig. 4.17. The most efficient heating case is shown to be the case with a weak magnetic field, 1 s period and higher amplitude. We observe that increasing the magnetic field also increases the damping effect, especially for high frequencies.

This limits the growth of the perturbation and reduces the non-linear effects, leading to a low efficient heating. A stronger perturbation also favours an efficient heating. Tests with large periods and large amplitude introduce several numerical effects and are still under study but, attending to the results, a stronger heating effect is expected in this case. Magnetoacoustic waves of larger periods are able to reach higher layers of the chomosphere, where the decoupling effects are more important, contributing to a larger increase in temperature.

5 Conclusions and future prospects

At the end of this work, we have learned about the difficulties of the study of two-fluid solutions from the analytic and numerical point of view. The possibility to obtain 1D analytic solutions in the case of single-fluid is even complicated when we introduce the magnetic field. The possibility to use the Mancha3D-2F code, which allows us to solve two-fluid and single-fluid equations was key for a deep comprehension of the results. We could test solutions in realistic environments, like the VAL-C model, an empirical model that describes the chromosphere, but we are still far from a realistic representation of the complexity of chromospheric processes.

The analysis of the homogeneous atmosphere shows that the two-fluid solution introduces two modes, a difference with the single-fluid one. In conditions of strong coupling, one of them (physical conditions can exchange the behaviour of modes) is quite similar to the expected for a single-fluid mode. In the two-fluid case, the mode has a spatial damping, with a damping scale that is large in comparison with the wavelength and the effect is not relevant in short distances. The length scale of the second mode is different in order of magnitude and the wave damps in a distance similar to the wavelength, and we can consider that the mode does not propagate. If the frequency of the perturbations is similar to the collisional frequency, the behaviour of both modes changes significantly: both wavelengths tend to be similar and the damping reaches a limit in growth. This can be understood as a first indication that the single-fluid solution is only valid to describe perturbations whose frequencies are much smaller than the collisional frequency.

The stratified atmosphere introduces a damping due to the solar gravity. We obtained a single-fluid approach to the analytic solution based on the local application of the isothermal solution. Since the gradients of temperature are small enough, the approximation allows us to check the numerical solution. For perturbations whose frequencies were similar to the collisional frequencies, we observed the two-fluid effects in the linear regime. We tested configurations with two values for the collisional cross-sections that can be found in the literature and observe important differences in the solutions, so a more detailed discussion must be done about the determination of this parameter.

It was not possible to reach frequencies large enough to observe reliable collisional effects in the study of acoustic shock waves. In the case of a perturbation with $\omega = 10s^{-1}$, we observe that the frictional heating becomes important for charges at high layers, so we believe that we are close to the region of interest.

The magnetic field introduces more relevant effects that allows us to detect differences between the two-fluid and single-fluid solutions at low frequencies. It also introduces a limitation on the period of the perturbation due to a strong increase of the damping. This effect vanishes the wave in the $\beta_{plasma} = 1$ region for a period of 1 s. This fact motivates us to obtain an analytic solution that explains the efficiency of the damping. The perturbation with 5 s period shows small differences between the two-fluid and single-fluid solutions whilst the perturbation with $T = 1s$ shows that the single-fluid solution grows in amplitude more than the single-fluid one and then both solutions vanish with the same amplitude. We conclude that the ambipolar damping is more efficient than the collisional damping. The ambipolar damping is strong enough to prevent non-linear effects and the formation of shock waves in conditions where two-fluid predicts them. More studies must be done to understand the limits of the ambipolar approach.

We were able to reproduce the results of Popescu Braileanu (2020) related with the collisional heating in presence of magnetic field. This justifies the motivation of the two-fluid approach: an explanation for the chomospheric heating. We also observe that perturbations that reach the upper layers of the chromosphere heat more efficiently due to the decrease of the collisional coupling.

The understanding of two-fluid solutions is not an easy task. Since the study of its equations leads

to systems of coupled equations, it is only possible to obtain analytic solutions in a few cases. This makes it difficult to distinguish between physical and numerical effects in the solutions. In future works, we will perform simulations for acoustic waves with non-linear effects and small amplitude to obtain a complete view of the collisional effects, for example, in the case with $\omega = 100s^{-1}$. For magnetoacoustic waves, we will study configurations with a constant magnetic field with $\vec{B}_0 \nparallel \hat{e}_z$ to observe effects of the magnetic tension. The case of a stratified magnetic field will be studied too. Ionizations and recombinations are frequent in the chromosphere, so the effects of the non-elastic collisional terms must be included and studied to pursue more realistic simulations.

Bibliography

Alvarez Laguna A., Lani A., Poedts S., Mansour N. N., Kosovichev A. G., 2014, in AGU Fall Meeting Abstracts. pp SH23A–4151

Ballester J. L., et al., 2018, , 214, 58

Berenger J.-P., 1994, Journal of Computational Physics, 114, 185

Biermann L., 1946, Naturwissenschaften, 33, 118

Bittencourt J. A., 2004, Fundamentals of Plasma Physics, third edn. Fundamentals of Plasma Physics, Third Edition by J.A. Bittencourt. Published by Springer-Verlag, New York, Inc.; 2004. ISBN 0-387-20975-1.

Braginskii S. I., 1965, Reviews of Plasma Physics, 1, 205

Carlsson M., Stein R. F., 2002, in Sawaya-Lacoste H., ed., ESA Special Publication Vol. 505, SOLMAG 2002. Proceedings of the Magnetic Coupling of the Solar Atmosphere Euroconference. pp 293–300

Centeno R., Collados M., Trujillo Bueno J., 2009, , 692, 1211

Cheung M. C. M., Cameron R. H., 2012, The Astrophysical Journal, 750, 6

Felipe T., Khomenko E., Collados M., 2010, , 719, 357

Gilbert H., Kilper G., Alexander D., 2007, , 671, 978

Goedbloed H., Keppens R., Poedts S., 2019, Magnetohydrodynamics of Laboratory and Astrophysical Plasmas. Cambridge University Press, doi:10.1017/9781316403679

Goldstein H., 1980, Classical Mechanics. Addison-Wesley

González-Morales P. A., Khomenko E., Downes T. P., de Vicente A., 2018, , 615, A67

Gough D. O., 2007, Astronomische Nachrichten, 328, 273

Gray D. F., 2005, Background, 3 edn. Cambridge University Press, doi:10.1017/CBO9781316036570.004

Hansen C., Kawaler S., 2012, Stellar Interiors: Physical Principles, Structure, and Evolution. Astronomy and Astrophysics Library, Springer New York, `https://books.google.es/books?id=oxjpBwAAQBAJ`

Hillier A., Takasao S., Nakamura N., 2016, , 591, A112

Kalkofen W., 2007, , 671, 2154

Khomenko E., Calvo Santamaria I., 2013, in Journal of Physics Conference Series. p. 012048 (`arXiv:1302.4351`), doi:10.1088/1742-6596/440/1/012048

Khomenko E., Collados M., 2006, , 653, 739

Khomenko E., Collados M., 2012, , 747, 87

Khomenko E., Collados M., 2015, Living Reviews in Solar Physics, 12, 6

Khomenko E., Collados Vera M., 2012, in Rimmele T. R., et al., eds, Astronomical Society of the Pacific Conference Series Vol. 463, Second ATST-EAST Meeting: Magnetic Fields from the Photosphere to the Corona.. p. 281 (arXiv:1202.2252)

Khomenko E., Collados M., Díaz A., Vitas N., 2014a, Physics of Plasmas, 21, 092901

Khomenko E., Díaz A., de Vicente A., Collados M., Luna M., 2014b, in Schmieder B., Malherbe J.-M., Wu S. T., eds, Vol. 300, Nature of Prominences and their Role in Space Weather. pp 90–93 (arXiv:1310.7016), doi:10.1017/S174392131301079X

Khomenko E., Collados M., Shchukina N., Díaz A., 2015, , 584, A66

Khomenko E., Collados M., Díaz A. J., 2016, , 823, 132

Khomenko E., Vitas N., Collados M., de Vicente A., 2017, , 604, A66

Khomenko E., Vitas N., Collados M., de Vicente A., 2018, , 618, A87

Leake J. E., Lukin V. S., Linton M. G., Meier E. T., 2012a, , 760, 109

Leake J. E., Lukin V. S., Linton M. G., Meier E. T., 2012b, The Astrophysical Journal, 760, 109

Leake J. E., Lukin V. S., Linton M. G., 2013, Physics of Plasmas, 20, 061202

Lukin V. S., Leake J., Linton M., 2013, in AGU Fall Meeting Abstracts. pp SH23A–2085

Maneva Y., Alvarez Laguna A., Lani A., Poedts S., 2017, in EGU General Assembly Conference Abstracts. EGU General Assembly Conference Abstracts. p. 16982

Martínez-Gómez D., Soler R., Terradas J., 2017, , 837, 80

Martínez-Sykora J., De Pontieu B., Hansteen V., 2012, , 753, 161

Mihalas D., 1978, Stellar Atmospheres. Astronomy and Astrophysics Series, W. H. Freeman

Osterbrock D. E., 1961, , 134, 347

Popescu Braileanu B., 2020, PhD thesis, University of La Laguna

Popescu Braileanu B., Lukin V. S., Khomenko E., de Vicente Á., 2019a, , 627, A25

Popescu Braileanu B., Lukin V. S., Khomenko E., de Vicente Á., 2019b, , 630, A79

Schwarzschild M., 1948, , 107, 1

Shelyag S., Khomenko E., de Vicente A., Przybylski D., 2016, , 819, L11

Smith P. D., Sakai J. I., 2008, , 486, 569

Vernazza J. E., Avrett E. H., Loeser R., 1981, , 45, 635

Vranjes J., Krstic P. S., 2013, , 554, A22

Zaqarashvili T. V., Khodachenko M. L., Rucker H. O., 2011, , 534, A93

de la Cruz Rodríguez J., Socas-Navarro H., 2011, , 527, L8